

# Estimation of Direction of Arrival by Time Reversal for Low-Angle Targets

XIAOLU ZENG ,  
MINGLEI YANG , Member, IEEE  
BAIXIAO CHEN

Xidian University, Xi'an, China

YUANWEI JIN , Senior Member, IEEE  
University of Maryland Eastern Shore, Princess Anne, MD, USA

In a low-angle target parameter estimation scenario, the backscattered signals from targets are often distorted due to clutter and multipath, which significantly degrades the performance of direction-of-arrival (DOA) estimation. In general, the backscattered multipaths are modeled as coherent signals with respect to the direct path. Decorrelation algorithms such as spatial smoothing and matrix reconstruction can mitigate the effect of multipath. However, most of these methods will perform poorly or even fail for solving parameter estimation problem of low-angle targets in complex terrain where there are rich multipath scatterings. This paper presents a novel method that combines time reversal (TR) technique, coherent signal-subspace method (CSM), and multiple signal classification algorithm to perform DOA estimation in a low-angle target scenario. The TR technique takes advantage of multipath echoes recorded by a sensor array and adaptively adjusts TR probing waveforms to increase the signal-to-noise ratio in a rich scattering environment. Moreover, the CSM method compresses the energy of a signal into a predefined subspace to exploit the full time-bandwidth product of signal sources and cope with coherent wavefronts. As a result, the proposed new DOA estimation

Manuscript received May 8, 2017; revised December 10, 2017 and March 30, 2018; released for publication April 4, 2018. Date of publication April 18, 2018; date of current version December 5, 2018.

DOI. No. 10.1109/TAES.2018.2828200

Refereeing of this contribution was handled by A. Martone.

This work was supported in part by the National Natural Science Foundation of China under Grant 61571344 and in part by the Fund for Foreign Scholars in University Research and Teaching Program (111 Project B18039).

Authors' addresses: X. Zeng, M. Yang, and B. Chen are with the National Laboratory of Radar Signal Processing and the Collaborative Innovation Center of Information Sensing and Understanding, Xidian University, Xi'an 710071, China, E-mail: (feiy3709@sina.com; mlyang@xidian.edu.cn; bxchen@xidian.edu.cn); Y. Jin is with the Department of Engineering and Aviation Sciences, University of Maryland Eastern Shore, Princess Anne, MD 21853 USA, E-mail: (yjin@umes.edu). (Corresponding author: Minglei Yang.)

This paper has supplementary downloadable material available at <http://ieeexplore.ieee.org>.

algorithm outperforms significantly the conventional methods. The Cramer–Rao bounds analysis and numerical simulations commendably validate the accuracy and robustness of the proposed method.

## I. INTRODUCTION

### A. Overview of Time Reversal (TR) for Direction-of-Arrival (DOA) Estimation

Very high-frequency (VHF) radar is often utilized to detect and localize low-angle targets because of its advantages of antistealth and anti-antiradiation missile properties [1]–[3]. Generally, echoes observed at an antenna array are recorded and processed to estimate the direction of a target relative to the antenna array. However, backscattered signals from the target will be distorted by clutter and multipath in the low-angle target estimation and tracking scenario in complex terrains [4]. Thus, the received echoes will have significant time spreads because their constituent signal components travelling along multiple propagation paths with different arrival times, amplitudes, and DOAs [5]. As a result, multipath makes it difficult to accurately extract the target information from noisy measurement data for DOA estimation. For conventional direct-path-based DOA estimators, multipath is either ignored [1], [6] or considered detrimental to the DOA estimation performance [3], [7]. In practice, the precision of DOA estimation will degrade significantly if the multipath effect is not dealt with properly. However, it is often difficult to eliminate (or mitigate) the effect of multipath using channel equalization or other filtering techniques especially at low signal-to-noise ratio (SNR) [8]–[10]. A natural question rises as what performance gain can be achieved if we exploit the target or channel information contained in multipath signals. Recently, researchers have shown that the TR method provides a unique paradigm that enables the constructive utilization of multipath to mitigate signal distortions [11], [12], and its practical implementation has become possible in areas such as acoustics [11], [13], [14], wireless networks [15], radio therapy medicines [16], and radar systems [8]. In particular, a wide variety of applications by TR in radar systems have been studied, for example, TR array imaging [17], target detection by TR [18], [19], TR multipleinput multipleoutput (TR-MIMO) radar [20], [21], and target classification [22]–[24].

For a typical TR experiment, an active antenna array first transmits a probing signal to the target. It then receives a superposition of several attenuated and delayed signals (called forward-echo for simplicity) reflected through a rich scattering medium from the target. Many conventional DOA estimation algorithms directly use the forward-echo to localize the target. However, in the TR method, the forward-echo is time reversed, energy normalized, and retransmitted through the same medium. The backscattered signals are received by the antenna sensors. In reference to the forward-echo, we call the backscattered signal in the TR method as TR-Echo. Many TR-based algorithms, including our recent work [25], utilize TR-Echo for target localization and classification [8], [20]. In these methods, the scattering environment is considered as reciprocal and multipath

rich. Therefore, time reversed signals that travel through the same background medium undergo similar scattering as that in the forward propagation step. Finally, they refocus on the original source. In array signal processing, the TR technique utilizes multipaths to increase the effective aperture and SNR; thereby, resulting in tighter temporal/spatial focusing and improving the target localization accuracy [8]. In a sense, the TR method makes the DOA estimators effective in multipath rich complex scenarios.

The TR-based DOA estimation problem in radar applications has been studied in literature (e.g., [8], [20]), in which the TR method exploits the spatial diversity arising from multipath propagation to improve the DOA estimation performance. In [8], the TR method garners the benefit of spatial/multipath diversity by incorporating all the multipath signal components associated with the intended target. A wideband TR-based Capon beamforming algorithm is studied in [8] that shows much improved estimation accuracy than the conventional Capon DOA estimator. A similar performance gain is also observed in a MIMO radar setting [20], in which the TR method enables adaptive waveform shaping for MIMO radar. Furthermore, singular value decomposition (SVD) based method, for example, the well-known multiple signal classification (MUSIC) algorithm [26]–[28], has also been studied in combination with the TR technique. Researchers use the eigenstructure of the TR observation matrix to locate the target, which results in the corresponding TR-MUSIC algorithms [29]–[32].

The DOA estimation for low-angle radar targets is a difficult task. This is because the radiation scattered by the target is reflected by the ground to the radar antennas. As a result, the direct return is mixed with coherent scattered return signals. The coherent scattered signals add constructively or destructively, which calls for coherent processing of the scattered radar signals to achieve high DOA estimation resolution. Furthermore, the DOA estimation accuracy is also related to the bandwidth of the radar signals [33]–[35]. For a low-angle target estimator by a VHF radar that typically operates in the frequency range of 30 to 300 MHz [1]–[3], the relative bandwidth of the radar signal is large. Thus, the existing TR-based DOA estimation algorithms discussed above are inadequate because they all rely on incoherent processing of wideband signals by either the incoherent TR Capon algorithm [8] or the subspace-based TR-MUSIC [29]. In particular, the classic incoherent subspace method (ISM) [36] first decomposes wideband signals into many narrowband signals and separately processes them at each frequency bin. The results are then combined incoherently to produce the final DOA estimation. However, this approach cannot localize coherent sources or closely separated targets in a low SNR scenario due to poor resolution [33]. To solve this problem, the coherent signal-subspace method (CSM), also named as focusing technique [33], constructs a single focusing frequency for wideband plane waves to obtain higher resolution. Essentially, in the CSM-based MUSIC algorithm [33], an SVD is applied only once into a focusing frequency data matrix over the entire bandwidth. For the incoherent

MUSIC algorithm, SVD operations must be done at each frequency bin, which becomes computationally prohibitive when the number of frequency bins is large. To address the challenges that rise from coherent and rich scattering multipath in wideband low-angle target DOA estimation, in this paper, we use the TR-MUSIC method in conjunction with the CSM method to achieve high resolution, high accuracy, and computationally efficient DOA estimation. In addition, our method is designed for coherent sources but it can also be used to locate incoherent targets with simple extension. Its superiorities in resolution and accuracy make it applicable for multiple target detection, localization, and tracking because they all fall in the category of DOA estimation that requires a good resolution and accuracy.

## B. Contributions of this Paper

The contributions of this paper are summarized as follows. First, we explore the concept of angle range of an impinging signal source that includes a direct path and rich multipaths from a low-angle target. By computing the effective specular and diffuse reflection areas, we develop a new reflection model in complex terrain for locating low-angle targets. Our model differs from the conventional low-angle reflection models for the VHF radar, in which multipath signals are approximated as a single multipath signal scaled by a complex coefficient [37]. By analyzing the distributions of multipath signals in specular and diffuse reflection areas of the antenna array, we show that the conventional treatment and modeling of multipath in a low-angle DOA estimation (e.g., [37]) is inadequate and inaccurate.

Second, we develop a new DOA estimation algorithm named [time reversal focusing spatial smoothing MUSIC (SSMUSIC)] (TRF-SSMUSIC) algorithm by jointly utilizing the TR method, the CSM focusing method, and the SSMUSIC [26], [38] for wideband DOA estimation in a low-angle scenario. Unlike our prior work in which the target is assumed to be stationary [25], we consider the scenario of moving targets and analyze the impact of Doppler shift in the TR-based signal model. The TR technique is adopted here to account for the rich multipath effect in order to improve the SNR. Wideband probing signals and the CSM method, which compresses the signal in a predefined subspace, are utilized to improve the resolution and accuracy of the TR DOA estimator. Specifically, we take the two-side correlation transformation (TCT) method [39] to execute the focusing process because it does not require preliminary DOA estimation [40] that is different from other focusing methods, such as the rotational signal subspace (RSS) [41] and the total least squares [34]. This feature of the TCT algorithm is very important because for low-angle targets, direct and multipath signals are closely separated, which makes the preliminary DOA estimation inaccurate. Hence, it will degrade the performance of the final DOA estimator. After focusing by the TCT, the SSMUSIC algorithm is utilized to perform the DOA estimation because of its super resolution. Unlike [8], which only uses the TR technique, we utilize both the TR technique and the TCT

focusing method. The TR technique inherently adapts the probing waveform to the scattering environment. The TCT focusing method exploits the full time-bandwidth product of sources to cope with coherent wavefronts [42]. As a result, our method achieves a better DOA estimation performance for low-angle targets by a VHF radar system than conventional methods.

Third, we derive the analytical expressions of Cramer-Rao bounds (CRB) for both conventional and TR-based DOA estimation algorithms based on our frequency-domain signal model. This is to verify the effectiveness of the TR technique for low-angle targets in a rich multipath environment. Numerical simulations are conducted to compare the performance of our TRF-SSMUSIC algorithm with other five benchmark algorithms, i.e., the conventional focusing SSMUSIC (CF-SSMUSIC) algorithm, the conventional wideband-Capon (C-SSCapon) method, the TR-based wideband-Capon method (TR-SSCapon) [8], [43], the conventional RSS focusing (C-RSSFocus) method, and the TR-based RSS focusing method (TR-RSSFocus) [41]. Numerical simulations demonstrate that the proposed TRF-SSMUSIC algorithm outperforms the benchmark algorithms in terms of accuracy and resolution in the DOA estimation.

This paper is organized as follows. In Section II, we analyze the angle range in low-angle scenarios and establish signal models for the TR-based DOA estimation problem. Section III derives the proposed TRF-SSMUSIC algorithm and introduces other competing algorithms. Error analysis of the TR DOA estimator is presented in Section IV. In Section V, numerical experiments are shown to verify our algorithm. Finally, Section VI concludes this paper.

## II. SIGNAL MODEL AND PROBLEM FORMULATION

### A. Angle Range for a Low-Angle Target

To establish the signal model with rich multipaths, we begin by analyzing the angle range that characterizes the DOAs of direct and multipath signals scattered from low-angle targets. The angle range of the impinging sources is related to the reflection area that is determined by the exact geometrical relationships between the target, ground, and the radar antenna. From the antenna and electromagnetic wave propagation theory [44], both the specular and diffuse reflection areas can be approximated as ellipses (see Fig. 1). In Fig. 1,  $H_R$  and  $H_T$ , respectively, denote the altitude of the radar and the target.  $D$  is the horizontal distance between the antenna and the target. Details of how to compute the geometric parameters of the specular and diffuse reflection areas are presented in [44] and the references therein.

Let  $\theta_{\text{Direct}}$ ,  $\theta_{\text{Specular}}$ ,  $\theta_{\text{Diffuse}}$  denote the angle of the direct path and multipath signals reflected from the specular and diffuse areas, respectively. Let us assume the reflection surface is flat, it is evident that the geometrical reflect point  $P$  on the ground is unique once  $D$ ,  $H_R$ , and  $H_T$  are fixed. In other words, multipaths reflected from the diffuse area cannot be received by the antenna array. Thus, only  $\theta_{\text{Direct}}$  and  $\theta_{\text{Specular}}$  exist in this case, which can be calculated eas-

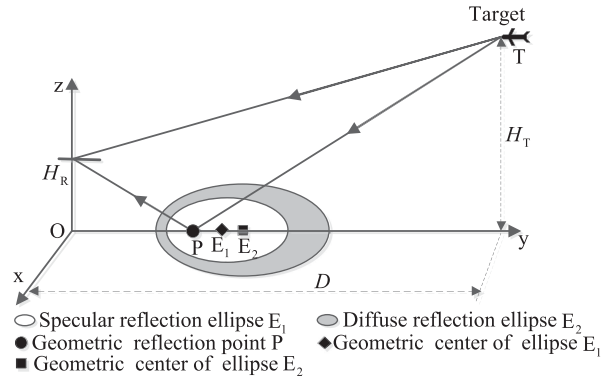


Fig. 1. Reflection area in a low-angle scenario.

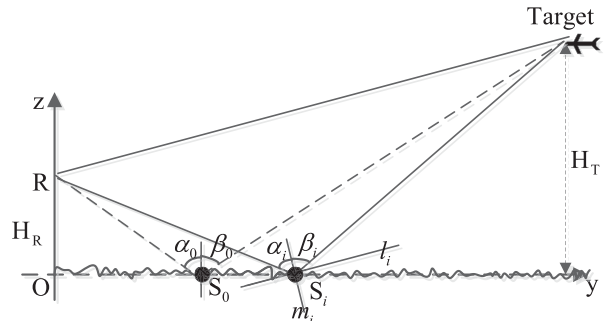


Fig. 2. Reflection model in a complex terrain.

ily from the geometrical relationships between the target, ground, and the radar antenna.

In practice, however, there are many types of terrain, such as rugged mountains and rough seas, where the reflection surfaces are no longer flat. In this case, there are multiple reflection points on the ground, thus causing multipath signals. Fig. 2 shows the reflection model in a complex terrain in which the reflection planes are slopes in some special positions between the array antenna and the target. In Fig. 2,  $S_0$  denotes the geometrical reflection point and  $S_i$  represents the reflection point different from  $S_0$ .  $l_i$  and  $m_i$  represent the tangent plane and normal line in  $S_i$ , respectively. From the antenna propagation theory [44], the antenna can receive signals (i.e., multipath signals) reflected from  $S_i$  once  $\alpha_i = \beta_i$  holds, which is often possible for low-angle targets in complex terrain.

Next, we analyze specular and diffuse reflection areas in complex terrain to compute the angle range of the impinging sources. Fig. 3(a) shows the specular and diffuse reflection areas versus different antenna array heights (i.e.,  $H_R = 4, 8, 12$  m) while the target altitude is 10 km. Similarly, Fig. 3(b) illustrates the specular and diffuse reflection areas versus different target heights (i.e.,  $H_T = 8, 9, 10$  km) while the antenna array height  $H_R$  is 8 m. In Fig. 3, the horizontal distance between the target and the receive antenna is 200 km, the carrier frequency is 200 MHz, and the corresponding beamwidth in azimuth and elevation is  $\phi_\alpha = 5^\circ$  and  $\phi_e = 3^\circ$ , respectively. It is obvious that the geometrical reflection points on the ground with symbol \* are not the center of these ellipses and they are closer to the receive

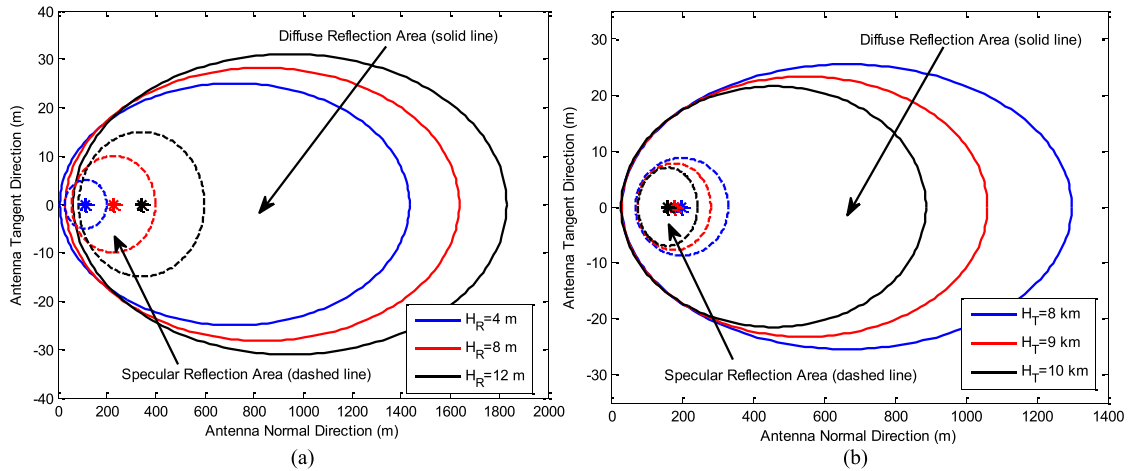


Fig. 3. Specular and diffuse reflection areas. (a) Reflection areas for different antenna heights. (b) Reflection areas for different target heights.

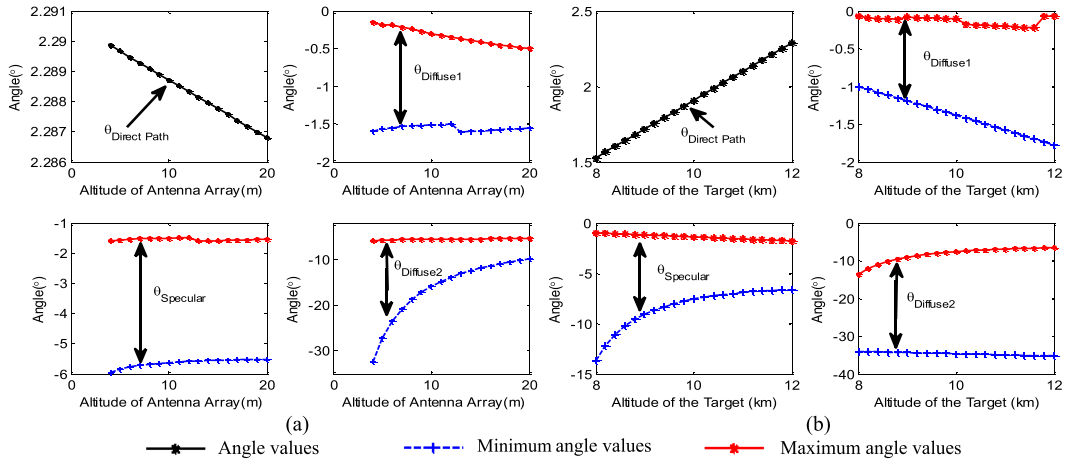


Fig. 4. Angle Range. (a) Angle versus antenna altitude. (b) Angle versus target altitude.

antenna than the centers. It can be easily seen from Fig. 3 that the specular reflection area is smaller than the diffuse reflection area for the same antenna and target altitudes.

Our analysis shows that the reflection points  $S_i$  on the ground are not only the geometrical reflection points but a set of reflection points due to the complex terrain (see Fig. 2). Moreover, Fig. 3 shows that the diffuse reflection area is segmented by the specular reflection area. Next, we decompose the diffuse reflection area into two parts: Area<sub>1</sub> and Area<sub>2</sub> which represent the diffuse area close to and far away from the antenna, respectively. Correspondingly, angles of the multipaths reflected from Area<sub>1</sub> and Area<sub>2</sub> are denoted as  $\theta_{Diffuse1}$  and  $\theta_{Diffuse2}$ , respectively. Then,  $\theta_{Diffuse}$  is given by  $\theta_{Diffuse_1} \cup \theta_{Diffuse_2}$ , where  $A \cup B$  denotes the union of set  $A$  and  $B$ . It is straightforward to calculate  $\theta_{Direct}$ ,  $\theta_{Specular}$ , and  $\theta_{Diffuse}$ , given the geometrical parameters of both specular and diffuse reflection areas [44].

Suppose the fluctuation of the reflection terrain obeys the Gaussian distribution [1], [2] with zero mean and variance 1 m. Fig. 4(a) and (b) depict the angle ranges versus different antenna array heights and target altitudes, respectively. From Fig. 4, we see that  $\theta_{Direct}$  is about  $2^\circ$ ,

$\theta_{Specular}$  is between  $-6^\circ$  and  $-2^\circ$ , while  $\theta_{Diffuse}$  is within  $-30^\circ \sim -6^\circ$  and  $-2^\circ \sim -0.1^\circ$ . The direct signal and the specular multipath signal fall within the same beamwidth of the receiving antenna in VHF radars. This observation is consistent with the result in [1]–[3]. Thus, high angular resolution is necessary in DOA estimation for low-angle targets. Furthermore, from the angle range of  $\theta_{Diffuse}$ , we conclude that multipath signals are widely distributed. Therefore, the conventional approach (e.g., [1]–[3]) that models the multipath signals as a multipath signal scaled by a complex coefficient is inaccurate and inadequate. Our approach by employing the TR method exploits the multipath signals to their advantages to improve the DOA estimation performance.

## B. Signal Model and Problem Formulation

In this section, we introduce our underlying hypothesis followed by the signal model. Fig. 5 illustrates the geometry of reflection for the TR using a uniform linear array (ULA) of  $M$  elements, denoted by  $A$ . We consider a target that is far from array  $A$ , so that the far-field approximation

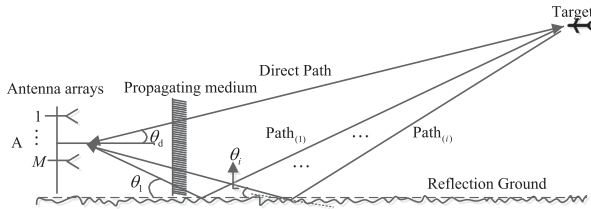


Fig. 5. Illustration of the signal reflection geometry for the TR DOA estimation.

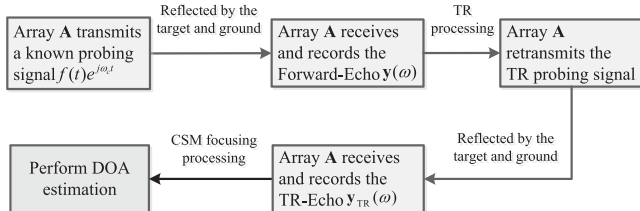


Fig. 6. Signal transmission scheme of the TR-based DOA estimator.

is applicable. It is also assumed to be a low-angle target with  $P$  scattered signal sources that include one direct path and  $P - 1$  multipaths. For a typical VHF radar, the velocity of a target of interest is usually  $v \leq 900$  m/s (about three times of the sound speed in air). The propagation environment is assumed to remain unchanged in the entire probing stage and the reciprocity condition holds. Furthermore, the signal source number  $P$  is assumed to be known a-priori. Note that the estimation of the number of sources is a classical problem in array signal processing [45]–[48]. We also assume that all the elements of array A transmit a known complex bandpass probing signal  $f(t)e^{jw_c t}$  to the channel simultaneously, where  $w_c$  is the angular carrier frequency.

Fig. 6 depicts the signal transmission scheme of the TR-based estimator in a single-base array radar system. A probing signal is transmitted by array A and backscattered by the target. Next, the original transmitting array A is switched to the receiving mode, which receives a superposition of scaled, time-delayed echoes of the probing signal by multipaths, resulting from the random multipath medium. The backscatter signal recorded by element  $k$  ( $1 \leq k \leq M$ ) of array A after down conversion to baseband and sampling can be expressed as [8], [49]

$$r_{(n,k)}(t) = \sum_{p=1}^P X_{(n,k,p)} f(t - \tau_{(n,p,1)} - \Delta\tau_{(k,1,p)}) e^{-j\omega_p t} + v_{(n,k)}(t) \quad (1)$$

where  $t = t_1, t_2, \dots, t_N$  and  $N$  is the number of snapshots. The Doppler frequency is  $\omega_p = \omega_c \beta_p$  with  $\beta_p = v_p/c$ , while  $c$  denotes the propagation velocity of the signal and  $v_p$  represents target velocity along multipath  $p$ . Let  $A_n$  and  $A_k$  denote the  $n$ th and  $k$ th element of array A, respectively.  $X_{(n,k,p)}$  denotes the synthetic path attenuation factor of the backscatter component traveling from element  $A_n$  to  $A_k$  via path  $p$ . Subscript  $(n, k, p)$  in (1) denotes the back scattered signal component that is transmitted by element  $A_n$ , backscattered by the target through path  $p$ ,

and finally recorded by element  $A_k$ .  $\tau_{(n,p,1)}$  is the reference propagation delay between the transmitting element  $A_n$  and the reference receiving element  $A_1$ , while  $\Delta\tau_{(k,1,p)}$  denotes the interelement delay of element  $A_k$  associated with path  $p$  in excess of the reference delay  $\tau_{(n,p,1)}$ . The symbol  $v_{(n,k)}(t)$  denotes the additive spatial and temporal Gaussian white noise with power spectral density of  $\sigma_v^2$ . By the far-field approximation, the attenuation factor  $X_{(n,k,p)}$  is assumed to be the same for all array elements, i.e.,  $X_{(n,k,p)} = X_p$ ,  $1 \leq n, k \leq M$ . Furthermore, we concentrate on the colocated array with an interelement spacing less than half of the wavelength of the probing signal, thus, the array size is much smaller than the target range distance. As a result, the reference propagation delay  $\tau_{(n,p,1)}$  via path  $p$  is approximately the same for all array elements, i.e.,  $\tau_{(n,p,1)} \approx \tau_{(p,1)}$ ,  $1 \leq n \leq M$ . Then, (1) can be rewritten as

$$r_k(t) = \sum_{p=1}^P X_p f(t - \tau_{(p,1)} - \Delta\tau_{(k,1,p)}) e^{-j\omega_p t} + v_k(t). \quad (2)$$

Since all of the multipath components are reflected from the same target, they can be regarded as coherent sources if  $|\tau_{(p_1,1)} - \tau_{(p_2,1)}| \leq \tau_R$  holds [50], where  $p_1, p_2 = 1, 2, \dots, P$  with  $p_1 \neq p_2$  and  $\tau_R = 1/B$ ,  $B$  is the bandwidth of the probing signal. In the frequency domain, (2) can be expressed as

$$R_k(\omega) = \sum_{p=1}^P X_p F(\omega + \omega_p) e^{-j\omega\tau_{(p,1)}} e^{-j\omega\Delta\tau_{(k,1,p)}} + V_k(\omega) \quad (3)$$

$$\approx \sum_{p=1}^P X_p F(\omega) e^{-j\omega\tau_{(p,1)}} e^{-j\omega\Delta\tau_{(k,1,p)}} + V_k(\omega) \quad (4)$$

where symbols  $F(\omega)$ ,  $R_k(\omega)$ ,  $V_k(\omega)$  are the discrete Fourier transforms of  $f(t)$ ,  $r_k(t)$  and  $v_k(t)$ , respectively. Note that our problem is to estimate the DOA rather than the velocity of the target. Let  $v_p$  denote the projection of  $v$  along the  $p$ th multipath direction, then  $v_p = v \cos \theta_p \leq v$  holds. It is safe to say the Doppler frequency  $\omega_p$  can be omitted. The validity of the approximation in (4) is analyzed in Appendix A based on the characteristics of wideband probing signals. We show in Appendix A that this approximation is closely related to the probing signal, target size, and sampling rate in the frequency domain. Interested readers can refer to other analysis methods, such as physical optics [51], [52] and electromagnetic waves [53], [54]. Note that this assumption has also been commonly used by other researchers (see e.g., [8], [49]) in DOA estimation. This approximation is very important to our TR-based DOA estimator. If the target moves very fast during the entire process, then the TR probing signal may not refocus on the target, which will undoubtedly result in DOA estimation errors.

We rewrite (4) in a compact matrix form as

$$\begin{aligned} \begin{bmatrix} R_1(\omega) \\ \vdots \\ R_M(\omega) \end{bmatrix}_{\mathbf{y}(\omega)_{M \times 1}} &= \underbrace{\begin{bmatrix} \mathbf{a}(\theta_1) \\ \vdots \\ \mathbf{a}(\theta_P) \end{bmatrix}^T_{\mathbf{A}(\Theta)_{M \times P}}} \underbrace{\begin{bmatrix} \mathbf{X}_{(1)} & & \\ & \ddots & \\ & & \mathbf{X}_{(P)} \end{bmatrix}_{\mathbf{X}_{P \times P}}} \\ &\times \underbrace{\begin{bmatrix} e^{-j\omega\tau_{(1,1)}} \\ \vdots \\ e^{-j\omega\tau_{(P,1)}} \end{bmatrix}_{\Gamma(\omega)_{P \times 1}}} \cdot \mathbf{F}(\omega) + \begin{bmatrix} \mathbf{v}_1(\omega) \\ \vdots \\ \mathbf{v}_M(\omega) \end{bmatrix}_{\mathbf{v}(\omega)_{M \times 1}}. \quad (5) \end{aligned}$$

Using the vector-matrix notations shown in (5) and considering all of the  $M$  elements of the array,  $\mathbf{y}(\omega)$  can be written by

$$\mathbf{y}(\omega) = \mathbf{A}(\Theta, \omega) \mathbf{X} \Gamma(\omega) \mathbf{F}(\omega) + \mathbf{v}(\omega) \quad (6)$$

where  $\mathbf{y}(\omega)$  is the frequency form of the forward-echo  $\mathbf{y}(t)$ . In (6),  $\Theta = [\theta_1, \theta_2, \dots, \theta_P]$ ,  $\mathbf{A}(\Theta, \omega)$ ,  $\mathbf{X}$  and  $\Gamma(\omega)$  denote the steering vector matrix, the synthetic path attenuation factor matrix, and the reference propagation delay vector, respectively.  $\mathbf{A}(\Theta, \omega)$  is a  $M \times P$  order matrix given in (7) as shown at the bottom of this page.  $d$  denotes the interelement spacing.

Next we derive the TR-Echo from forward-echo presented in (6). According to Fig. 6, the forward-echo (i.e.,  $\mathbf{y}(\omega)$ ) is digitized, energy normalized, time-reversed (equivalent to phase conjugation in the frequency domain), and retransmitted to the medium. The signal is reflected by the target and backscattered to array A. Similar to (6), the TR received signal, called TR-Echo  $\mathbf{y}_{\text{TR}}(\omega)$ , is given by

$$\mathbf{y}_{\text{TR}}(\omega) = \sum_{m=1}^M \mathbf{A}(\Theta, \omega) \mathbf{X} \Gamma(\omega) \mathbf{z}_m(\omega) + \mathbf{n}(\omega) \quad (8)$$

where  $\mathbf{z}(\omega) = g\mathbf{y}^*(\omega)$  denotes the TR probing signal vector,  $\mathbf{z}_m(\omega)$  refers to the  $m$ th entry of  $\mathbf{z}(\omega)$ , and  $\mathbf{n}(\omega)$  denotes the total noise in both conventional and TR probing process.  $g$  is the energy normalization factor, which can be computed by

$$g = \sqrt{(\|\mathbf{F}(\omega)\|^2) / (\|\mathbf{y}(\omega)\|^2)}. \quad (9)$$

Similar to (6), (8) can be expressed in the matrix format as

$$\mathbf{y}_{\text{TR}}(\omega) = \mathbf{A}_{\text{TR}}(\Theta, \omega) \mathbf{X}_{\text{TR}} \Gamma_{\text{TR}}(\omega) \mathbf{Z}_{\text{TR}}(\omega) + \mathbf{n}(\omega). \quad (10)$$

In (10), the block matrix  $\mathbf{A}_{\text{TR}}(\Theta, \omega) = [\mathbf{A}(\Theta, \omega) | \mathbf{A}(\Theta, \omega) | \dots | \mathbf{A}(\Theta, \omega)]$  is of the order  $M \times MP$ , while  $\mathbf{X}_{\text{TR}} = \mathbf{I}_M \otimes \mathbf{X}$  is a square matrix with dimensions of  $MP \times MP$

$$\begin{aligned} \Gamma_{\text{TR}}(\omega) &= \mathbf{I}_M \otimes \text{diag}[\Gamma(\omega)], \\ \mathbf{Z}_{\text{TR}}(\omega) &= [\mathbf{z}_1(\omega) \mathbf{1}_M, \dots, \mathbf{z}_M(\omega) \mathbf{1}_M]^T \quad (11) \end{aligned}$$

where  $\otimes$  represents the Kronecker product. The operation  $\text{diag}[\Gamma(\omega)]$  represents a square matrix with elements of  $[\Gamma(\omega)]$  on the main diagonal.  $\mathbf{I}_M$  is a unit matrix of order  $M$  and  $\mathbf{1}_M$  refers to a row vector of dimension  $M$  with all entries equal to 1. Therefore, the problem of interest is to seek  $\hat{\Theta}$  from measurement data  $\mathbf{y}_{\text{TR}}(\omega)$  given in (10).

### III. PROPOSED TRF-SSMUSIC ALGORITHM

This section presents the TRF-SSMUSIC algorithm to solve the DOA estimation problem.

#### A. TRF-SSMUSIC Algorithm

Following (10), the spectrum of TR signal vector  $\mathbf{y}_{\text{TR}}(\omega)$  is divided into  $Q$  equally spaced frequency bins. The signal vector for a fixed frequency  $\omega_q$  is denoted as  $\mathbf{y}_{\text{TR}}(\omega_q)$ . The corresponding covariance matrix at the  $q$ th frequency bin can be written as

$$\mathfrak{R}_{\mathbf{y}}^{\text{TR}}(\omega_q) = \mathbb{E} \{ \mathbf{y}_{\text{TR}}(\omega_q) (\mathbf{y}_{\text{TR}}(\omega_q))^H \} \quad (12)$$

where  $q = 1, 2, \dots, Q$  and  $\mathbb{E}$  represents expectation operator.

The CSM algorithm transforms the signal into a pre-defined subspace at the focusing frequency  $\omega_0$  [33]. From [33], [39], the transformation process can be expressed as

$$\mathbf{T}_q(\omega_q) \mathfrak{R}_{\mathbf{y}}^{\text{TR}}(\omega_q) \mathbf{T}_q^H(\omega_q) = \mathfrak{R}_{\mathbf{y}}^{\text{TR}}(\omega_0) \quad (13)$$

where  $\mathbf{T}_q(\omega_q)$ ,  $q = 1, 2, \dots, Q$  denotes the transformation matrix at  $\omega_q$ . For notational simplicity, we omit the frequency variable by representing  $\mathbf{T}_q(\omega_q)$  as  $\mathbf{T}_q$  and  $\mathfrak{R}_{\mathbf{y}}^{\text{TR}}(\omega_q)$  as  $\mathfrak{R}_{\mathbf{y}}^{\text{TR}}(q)$ .

We note that if  $\omega_0$  is arbitrarily selected as the solution of (13), it may or may not fall in the range of  $\{\omega_1, \dots, \omega_Q\}$ . Therefore, we reformulate (13) into a constrained minimization problem to find a practical value of  $\omega_0$

$$\begin{aligned} \min_{\mathbf{T}_q} \| \mathfrak{R}_{\mathbf{y}}^{\text{TR}}(0) - \mathbf{T}_q \mathfrak{R}_{\mathbf{y}}^{\text{TR}}(q) \mathbf{T}_q^H \|_F \\ \text{s.t. } \mathbf{T}_q^H \mathbf{T}_q = \mathbf{I}, q = 1, 2, \dots, Q. \quad (14) \end{aligned}$$

---


$$\mathbf{A}(\Theta, \omega) = \begin{bmatrix} 1 & \dots & 1 & \dots & 1 \\ \vdots & \ddots & \vdots & \ddots & \vdots \\ e^{-j\Omega(m) \sin \theta_1} & \dots & e^{-j\Omega(m) \sin \theta_p} & \dots & e^{-j\Omega(m) \sin \theta_p} \\ \vdots & \ddots & \vdots & \ddots & \vdots \\ e^{-j\Omega(M-1) \sin \theta_1} & \dots & e^{-j\Omega(M-1) \sin \theta_p} & \dots & e^{-j\Omega(M-1) \sin \theta_p} \end{bmatrix}_{\mathbf{a}(\theta_1, \omega) \quad \mathbf{a}(\theta_p, \omega) \quad \mathbf{a}(\theta_p, \omega)} \quad \text{with } \Omega = \omega d/c. \quad (7)$$

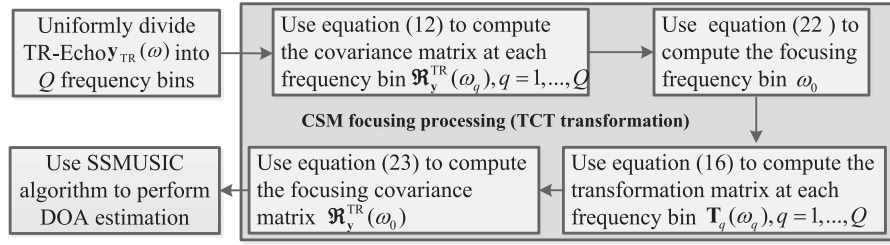


Fig. 7. Key steps and flow chart of the TRF-SSMUSIC algorithm.

In (14), symbol  $\|\cdot\|_F$  is the Frobenius norm defined by

$$\|\mathbf{B}\|_F = [\text{tr}(\mathbf{B}^H \mathbf{B})]^{\frac{1}{2}} \quad (15)$$

where  $\text{tr}(\cdot)$  stands for the trace of a matrix. From (14), we can obtain the transformation matrix  $\mathbf{T}_q$  at frequency bin  $\omega_q$  as

$$\mathbf{T}_q = \mathbf{U}(\omega_0) \mathbf{U}^H(\omega_q) \quad (16)$$

where  $\mathbf{U}(\omega_0)$  and  $\mathbf{U}^H(\omega_q)$  denote the eigenmatrices constructed by eigenvectors of  $\mathfrak{R}_y^{\text{TR}}(0)$  and  $\mathfrak{R}_y^{\text{TR}}(q)$ , respectively. The validity of (16) is given in Appendix B.

From (16), it is easy to see that the computation of  $\mathbf{T}_q$  relies on the focusing frequency  $\omega_0$ . Therefore, we first compute the focusing frequency  $\omega_0$  and then  $\mathbf{T}_q$  as shown in Fig. 7. Taking the focusing error into consideration, we define

$$\varepsilon = \min_{\omega_0} \min_{\mathbf{T}_q} \left\| \mathfrak{R}_y^{\text{TR}}(0) - \mathbf{T}_q \mathfrak{R}_y^{\text{TR}}(q) \mathbf{T}_q^H \right\|_F^2 \quad (17)$$

where  $\varepsilon$  represents the focusing error of all frequency bins. From (17), when  $\omega_0$  is fixed,  $\mathfrak{R}_y^{\text{TR}}(0)$  is also fixed. Then,  $\varepsilon$  can be rewritten as

$$\begin{aligned} \varepsilon = \min_{\omega_0} \min_{\mathbf{T}_q} \sum_{q=1}^Q & \left[ \left\| \mathfrak{R}_y^{\text{TR}}(0) \right\|_F^2 + \left\| \mathfrak{R}_y^{\text{TR}}(q) \right\|_F^2 \right. \\ & \left. - 2 \sum_{l=1}^L \sigma_l(\mathfrak{R}_y^{\text{TR}}(0)) \sigma_l(\mathfrak{R}_y^{\text{TR}}(q)) \right] \end{aligned} \quad (18)$$

where  $\sigma_l(\mathfrak{R}_y^{\text{TR}}(0))$  and  $\sigma_l(\mathfrak{R}_y^{\text{TR}}(q))$  represent the singular value of  $\mathfrak{R}_y^{\text{TR}}(0)$  and  $\mathfrak{R}_y^{\text{TR}}(q)$ , respectively.  $L$  is the number of nonzero singular values. Note that in (18),  $\mathfrak{R}_y^{\text{TR}}(q)$  is not related to  $\omega_0$ , thus, (18) can be rewritten as follows for simplified mathematical computation:

$$\varepsilon = \min_{\omega_0} \sum_{q=1}^Q \left[ \sum_{l=1}^L [\sigma_l^2(\mathfrak{R}_y^{\text{TR}}(0)) - 2\sigma_l(\mathfrak{R}_y^{\text{TR}}(0))\sigma_l(\mathfrak{R}_y^{\text{TR}}(q))] \right] \quad (19)$$

$$= \min_{\omega_0} \sum_{l=1}^L \left[ Q\sigma_l^2(\mathfrak{R}_y^{\text{TR}}(0)) - 2\sigma_l(\mathfrak{R}_y^{\text{TR}}(0)) \sum_{q=1}^Q \sigma_l(\mathfrak{R}_y^{\text{TR}}(q)) \right]. \quad (20)$$

The solution to (20) is given as follows (see also [39]):

$$\sigma_l(\mathfrak{R}_y^{\text{TR}}(0)) = \frac{1}{Q} \sum_{q=1}^Q \sigma_l(\mathfrak{R}_y^{\text{TR}}(q)) \quad (21)$$

where  $l = 1, 2, \dots, L$ . Note that, (21) is the theoretical value of  $\sigma_l(\mathfrak{R}_y^{\text{TR}}(0))$  that cannot always be obtained because the number of frequency bin  $Q$  is limited. The theoretical focusing frequency  $\omega_0$  may not fall in the frequency range of  $\omega_q$  with  $q = 1, 2, \dots, Q$ . Therefore, we replace (21) by the following equation as an approximation, i.e.,

$$\min_{\omega_0} \sum_{l=1}^L \left| \sigma_l(\mathfrak{R}_y^{\text{TR}}(0)) - \frac{\mu_l}{Q} \right|^2 \text{ with } \mu_l = \sum_{q=1}^Q \sigma_l(\mathfrak{R}_y^{\text{TR}}(q)). \quad (22)$$

Equation (22) is a one-variable optimization problem, and a search for the minimum can be performed to obtain the focusing frequency  $\omega_0$  conveniently.

Having obtained the focusing frequency  $\omega_0$  from (22) and inserting  $\omega_0$  into (16), we obtain transformation matrix  $\mathbf{T}_q$  at each frequency bin  $\omega_q$ . We then compute the focusing covariance matrix  $\mathfrak{R}_y^{\text{TR}}(0)$  by

$$\mathfrak{R}_y^{\text{TR}}(0) = \frac{1}{Q} \sum_{q=1}^Q \mathbf{T}_q \mathfrak{R}_y^{\text{TR}}(q) \mathbf{T}_q^H. \quad (23)$$

Next, we use the SSMUSIC method to perform the DOA estimation. It is well known that SSMUSIC is based on the covariance matrix of the observations that we have obtained in (23). The spatial smoothing technique is to recover the rank of the singular covariance matrix obtained from coherent signal sources. By spatial smoothing [38], the original array with  $M$  identical sensors is divided into  $K$  overlapping subarrays of size  $H$  with sensors  $\{1, 2, \dots, H\}$  forming the first subarray, sensors  $\{2, 3, \dots, H+1\}$  forming the second subarray. A simple calculation shows that  $H = M - K + 1$ . Note that  $K \geq P$  and  $H \geq P$  are two necessary conditions to ensure that the recovering covariance matrix, denoted as  $\{\mathfrak{R}_y^{\text{TR}}(\omega_0)\}_{\text{SS}}$ , is a full-rank matrix. For notational simplicity, we omit the detailed computation process of  $\{\mathfrak{R}_y^{\text{TR}}(\omega_0)\}_{\text{SS}}$ . Interested readers can refer to [38] for detailed discussion. Combing the full-rank matrix  $\{\mathfrak{R}_y^{\text{TR}}(\omega_0)\}_{\text{SS}}$  with SSMUSIC algorithm, the pseudospectrum of our proposed TRF-SSMUSIC algorithm can be

derived as

$$\mathbb{P}_{\text{TR}}(\theta) = \frac{1}{\mathbf{a}^H(\theta, \omega_0) \hat{\mathbf{U}}_N \hat{\mathbf{U}}_N^H \mathbf{a}(\theta, \omega_0)} \quad (24)$$

where  $\theta$  is the search angle. As defined previously in (7),  $\mathbf{a}(\theta, \omega_0)$  is the steering vector at focusing frequency  $\omega_0$ , given by

$$\mathbf{a}(\theta, \omega_0) = [1, e^{-j\Omega_0(1)\sin\theta}, \dots, e^{-j\Omega_0(M-1)\sin\theta}]^T \quad (25)$$

where  $\Omega_0 = \omega_0 d/c$ . Symbol  $\hat{\mathbf{U}}_N$  denotes the noise subspace that is spanned by the noise eigenvectors. Note that the noise eigenvectors here are actually the  $(M - P)$  small eigenvalues of  $\{\Re_y(\omega_0)\}_{\text{SS}}$ . The TRF-SSMUSIC algorithm plots  $\mathbb{P}_{\text{TR}}(\theta)$  as a function of  $\theta$  and determines the DOAs by choosing the values of  $\theta$  corresponding to  $P$  highest peaks in the pseudospectrum. The main steps and the processing flow of the algorithm are summarized in Fig. 7.

## B. CF-SSMUSIC Algorithm

Owing to the analogy between the proposed TRF-SSMUSIC algorithm and the CF-SSMUSIC algorithm, the conventional algorithm procedure follows similar steps to the TRF-SSMUSIC algorithm. The main modification is that the signal models for the TRF-SSMUSIC and CF-SSMUSIC algorithm are different, i.e., (10) and (6), respectively. Following (6), we denote the covariance matrix of the CF-SSMUSIC algorithm at the  $q$ th frequency bin as

$$\Re_y(\omega_q) = \mathbb{E} \{ \mathbf{y}(\omega_q) (\mathbf{y}(\omega_q))^H \}, q = 1, 2, \dots, Q. \quad (26)$$

Next, we execute the analogous focusing process and spatial smoothing procedure for (26). The final rank-recovered covariance matrix of the CF-SSMUSIC algorithm is expressed as  $\{\Re_y(\omega_0)\}_{\text{SS}}$ , which is different from  $\{\Re_y^{\text{TR}}(\omega_0)\}_{\text{SS}}$  derived in Section III-A. We then obtain the pseudospectrum of CF-SSMUSIC algorithm given by

$$\mathbb{P}(\theta) = \frac{1}{\mathbf{a}(\theta, \omega_0)^H \hat{\mathbf{E}}_N \hat{\mathbf{E}}_N^H \mathbf{a}(\theta, \omega_0)} \quad (27)$$

where  $\mathbf{a}(\theta, \omega_0)$  is the steering vector given by (25). Symbol  $\hat{\mathbf{E}}_N$  denotes the noise subspace that is spanned by the noise eigenvectors of  $\{\Re_y(\omega_0)\}_{\text{SS}}$ .

## IV. CRAMER–RAO LOWER BOUNDS

In this section, we derive CRBs for both conventional and TR DOA estimators based on the frequency signal model given in (6) and (10), respectively.

### A. TR CRB

Now we derive TR CRB by rewriting (10) as

$$\mathbf{y}_{\text{TR}}(\omega) = \mathbf{A}(\Theta) \mathbf{X} [\Gamma(\omega) | \Gamma(\omega) | \Gamma(\omega)] g \mathbf{y}^*(\omega) + \mathbf{n}(\omega) \quad (28)$$

$$= \underbrace{[\mathbf{h}(\Theta, \omega) | \mathbf{h}(\Theta, \omega) | \cdots | \mathbf{h}(\Theta, \omega)]}_{\mathbf{H}(\Theta, \omega)_{M \times M}} \times g \mathbf{A}^*(\Theta) \underbrace{\mathbf{X}^* \Gamma^*(\omega) \mathbf{F}^*(\omega)}_{\mathbf{s}_{\text{TR}}(\omega)} + \mathbf{n}(\omega) \quad (29)$$

$$= \mathbf{B}(\Theta, \omega) \mathbf{s}_{\text{TR}}(\omega) + \mathbf{n}(\omega) \quad (30)$$

$$= \mathbf{x}_{\text{TR}}(\omega) + \mathbf{n}(\omega) \quad (31)$$

where  $\mathbf{x}_{\text{TR}}(\omega) = \mathbf{B}(\Theta, \omega) \mathbf{s}_{\text{TR}}(\omega)$  and,  $\mathbf{h}(\Theta, \omega) = \mathbf{A}(\Theta) \mathbf{X} \Gamma(\omega)$ .  $\mathbf{s}_{\text{TR}}(\omega) = \mathbf{X}^* \Gamma^*(\omega) \mathbf{F}^*(\omega)$  denotes the TR signal vector.  $\mathbf{n}(\omega)$  is the additive, white Gaussian noise vector with power spectral density  $\sigma_v^2 \mathbf{I}_M$ .  $\mathbf{B}(\Theta, \omega)$  represents the steering vector in TR probing process given by

$$\begin{aligned} \mathbf{B}(\Theta, \omega) &= \mathbf{H}(\Theta, \omega) g \mathbf{A}^*(\Theta) \\ &= [\mathbf{b}(\theta_1, \omega), \mathbf{b}(\theta_2, \omega), \dots, \mathbf{b}(\theta_P, \omega)]. \end{aligned} \quad (32)$$

At frequency  $\omega_q$ ,  $q = 1, 2, \dots, Q$ , we obtain

$$\mathbf{y}_{\text{TR}}(\omega_q) = \mathbf{x}_{\text{TR}}(\omega_q) + \mathbf{n}(\omega_q). \quad (33)$$

By combining  $Q$  vectors  $\mathbf{y}_{\text{TR}}(\omega_q)$ ,  $\mathbf{x}_{\text{TR}}(\omega_q)$  and  $\mathbf{n}(\omega_q)$  into one vector, we obtain data vectors  $\mathbf{y}_{\text{TR}}^s$ ,  $\mathbf{x}_{\text{TR}}^s$ , and  $\mathbf{n}_s$  by

$$\begin{aligned} \mathbf{y}_{\text{TR}}^s &= [\mathbf{y}_{\text{TR}}(\omega_1)^T, \mathbf{y}_{\text{TR}}(\omega_2)^T, \dots, \mathbf{y}_{\text{TR}}(\omega_Q)^T]^T \\ \mathbf{x}_{\text{TR}}^s &= [\mathbf{x}_{\text{TR}}(\omega_1)^T, \mathbf{x}_{\text{TR}}(\omega_2)^T, \dots, \mathbf{x}_{\text{TR}}(\omega_Q)^T]^T \\ \mathbf{n}_s &= [\mathbf{n}^T(\omega_1), \mathbf{n}^T(\omega_2), \dots, \mathbf{n}^T(\omega_Q)]^T. \end{aligned} \quad (34)$$

As we have noted in (2),  $v_k(t)$  is a Gaussian white noise with power spectral density of  $\sigma_v^2$ ; thus,  $\mathbf{n}_s$  is also white Gaussian noise based on the central limit theorem [55]. The spectral density matrix of  $\mathbf{n}_s$  is

$$\mathbf{R} = \mathbb{E} (\mathbf{n}_s \mathbf{n}_s^T) = N \sigma_v^2 \delta_{q_1, q_2} \mathbf{I}_{MQ} \quad (35)$$

where  $N$  is the number of snapshots in the time domain,  $1 \leq q_1, q_2 \leq Q$  and  $\mathbf{I}_{MQ}$  is a unit matrix of  $MQ$  order. Therefore, the joint probability density functions of  $\mathbf{y}_{\text{TR}}^s$  is

$$p(\mathbf{y}_{\text{TR}}^s | \vartheta) = \frac{1}{\pi^{MQ}} \exp \left[ - (\mathbf{y}_{\text{TR}}^s - \mathbf{x}_{\text{TR}}^s)^H \mathbf{R}^{-1} (\mathbf{y}_{\text{TR}}^s - \mathbf{x}_{\text{TR}}^s) \right] \quad (36)$$

where  $\vartheta$  is a vector composed by parameters to be estimated that may include noise variance  $N \sigma_v^2$ , signal vector  $\mathbf{s}_{\text{TR}}(\omega_q)$ , and DOA vector  $\Theta = [\theta_1, \theta_2, \dots, \theta_P]$ . By substituting the wideband array model into (36) and taking the logarithm, we obtain the logarithm likelihood function

$$\begin{aligned} \ln L(\vartheta) &= MJ \ln(\pi) - MJ \ln(N \sigma_v^2) - \frac{1}{N \sigma_v^2} \sum_{q=1}^Q [\mathbf{y}_{\text{TR}}(\omega_q) \\ &\quad - \mathbf{B}(\Theta, \omega_q) \mathbf{s}_{\text{TR}}(\omega_q)]^H [\mathbf{y}_{\text{TR}}(\omega_q) \\ &\quad - \mathbf{B}(\Theta, \omega_q) \mathbf{s}_{\text{TR}}(\omega_q)]. \end{aligned} \quad (37)$$

By taking the second-order partial derivative of (37) and computing their mathematical expectations, we obtain the

nonzero elements of the Fisher information matrix. Then, the CRB of  $\Theta$  can be obtained as (see also [55])

$$\text{CRB}_{\text{TR}}(\Theta) = \frac{N\sigma_v^2}{2} \left\{ \sum_{q=1}^Q \text{Re} \left\{ \mathbf{S}_{\text{TR}}^H(\omega_q) \mathbf{D}_{\text{TR}}^H(\omega_q) [\mathbf{I} - \mathbf{P}_{\mathbf{B}}^{\text{TR}}] \right. \right. \\ \left. \left. \mathbf{D}_{\text{TR}}(\omega_q) \mathbf{S}_{\text{TR}}(\omega_q) \right\}^{-1} \right\} \quad (38)$$

where  $\mathbf{S}_{\text{TR}}(\omega_q)$ ,  $\mathbf{D}_{\text{TR}}(\omega_q)$ , and  $\mathbf{P}_{\mathbf{B}}^{\text{TR}}$  are

$$\mathbf{S}_{\text{TR}}(\omega_q) = \text{diag}[\mathbf{s}_{\text{TR}}(\omega_q)] \quad (39)$$

$$\mathbf{D}_{\text{TR}}(\omega_q) = \left[ \frac{\partial \mathbf{b}(\theta_1, \omega_q)}{\partial \theta_1}, \frac{\partial \mathbf{b}(\theta_2, \omega_q)}{\partial \theta_2}, \dots, \frac{\partial \mathbf{b}(\theta_P, \omega_q)}{\partial \theta_P} \right] \quad (40)$$

$$\mathbf{P}_{\mathbf{B}}^{\text{TR}} = \mathbf{B}(\Theta, \omega_q) [\mathbf{B}^H(\Theta, \omega_q) \mathbf{B}(\Theta, \omega_q)]^{-1} \mathbf{B}^H(\Theta, \omega_q). \quad (41)$$

In (38) and (40),  $\text{Re}\{\cdot\}$  denotes the real part of the parameter enclosed in the parenthesis and  $\text{diag}[\mathbf{s}_{\text{TR}}(\omega_q)]$  represents a square matrix with elements of  $\mathbf{s}_{\text{TR}}(\omega_q)$  on the main diagonal.

### B. Conventional CRB

Next, we derive the conventional CRB based on the forward-echo  $\mathbf{y}(\omega)$  in (6).  $\mathbf{y}(\omega)$  can be rewritten as

$$\mathbf{y}(\omega) = \mathbf{A}(\Theta, \omega) \mathbf{X} \Gamma(\omega) \mathbf{F}(\omega) + \mathbf{v}(\omega) \quad (42)$$

$$= \mathbf{A}(\Theta, \omega) \mathbf{s}(\omega) + \mathbf{v}(\omega) \quad (43)$$

$$= \mathbf{x}(\omega) + \mathbf{v}(\omega) \quad (44)$$

where  $\mathbf{x}(\omega) = \mathbf{A}(\Theta, \omega) \mathbf{s}(\omega)$ .  $\mathbf{s}(\omega) = \mathbf{X} \Gamma(\omega) \mathbf{F}(\omega)$  denotes the signal vector containing  $P$  sources.

Owing to the analogy between (31) and (44), we follow the process in (33)–(37) to derive the conventional CRB as follows [55]:

$$\text{CRB}(\Theta) =$$

$$\frac{N\sigma_v^2}{2} \left\{ \sum_{q=1}^Q \text{Re} \left\{ \mathbf{S}_{\text{TR}}^H(\omega_q) \mathbf{D}_{\text{TR}}^H(\omega_q) (\mathbf{I} - \mathbf{P}_{\mathbf{A}}) \mathbf{D}(\omega_q) \mathbf{S}(\omega_q) \right\}^{-1} \right\} \quad (45)$$

where  $\mathbf{S}(\omega_q)$ ,  $\mathbf{D}(\omega_q)$ , and  $\mathbf{P}_{\mathbf{A}}$  are given by

$$\mathbf{S}(\omega_q) = \text{diag}[\mathbf{s}(\omega_q)] \quad (46)$$

$$\mathbf{D}(\omega_q) = \left[ \frac{\partial \mathbf{a}(\theta_1, \omega_q)}{\partial \theta_1}, \frac{\partial \mathbf{a}(\theta_2, \omega_q)}{\partial \theta_2}, \dots, \frac{\partial \mathbf{a}(\theta_P, \omega_q)}{\partial \theta_P} \right] \quad (47)$$

$$\mathbf{P}_{\mathbf{A}} = \mathbf{A}(\Theta, \omega_q) [\mathbf{A}^H(\Theta, \omega_q) \mathbf{A}(\Theta, \omega_q)]^{-1} \mathbf{A}^H(\Theta, \omega_q). \quad (48)$$

## V. NUMERICAL SIMULATIONS

In this section, we conduct numerical simulations to verify the performance of our proposed TRF-SSMUSIC algorithm and compare it with the following five benchmark CF-SSMUSIC, C-SSCapon, TR-SSCapon [8], [43],

TABLE I  
Angle Range in Low-Angle Scenario

signal	Angle Range
$\theta_{\text{Direct}}$	$2^\circ$
$\theta_{\text{Specular}}$	$-5^\circ \sim -1.5^\circ$
$\theta_{\text{Diffuse}}$	$-5^\circ \sim -0.5^\circ, -30^\circ \sim -5^\circ$

TABLE II  
Parameters Used in the Monte Carlo Simulations

Number of antenna elements	16
Number of frequency bins	1000
1-path	Direction of arrival
	Time delays
	Attenuation factors
2-path	Direction of arrival
	Time delays
	Attenuation factors
3-path	Direction of arrival
	Time delays
	Attenuation factors
4-path	Direction of arrival
	Time delays
	Attenuation factors

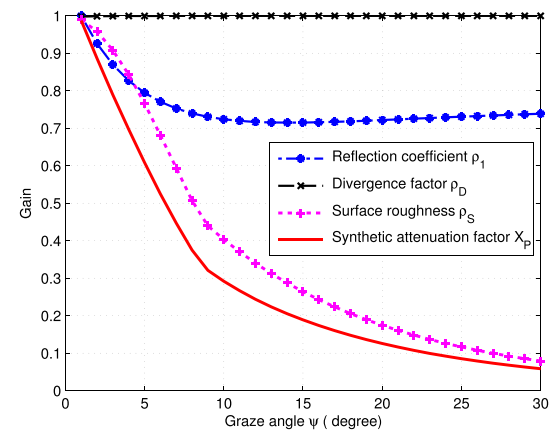


Fig. 8. Synthetic path attenuation factor.

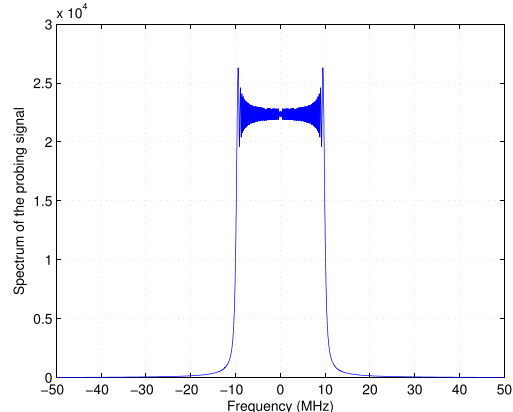


Fig. 9. Spectrum of the probing signal.

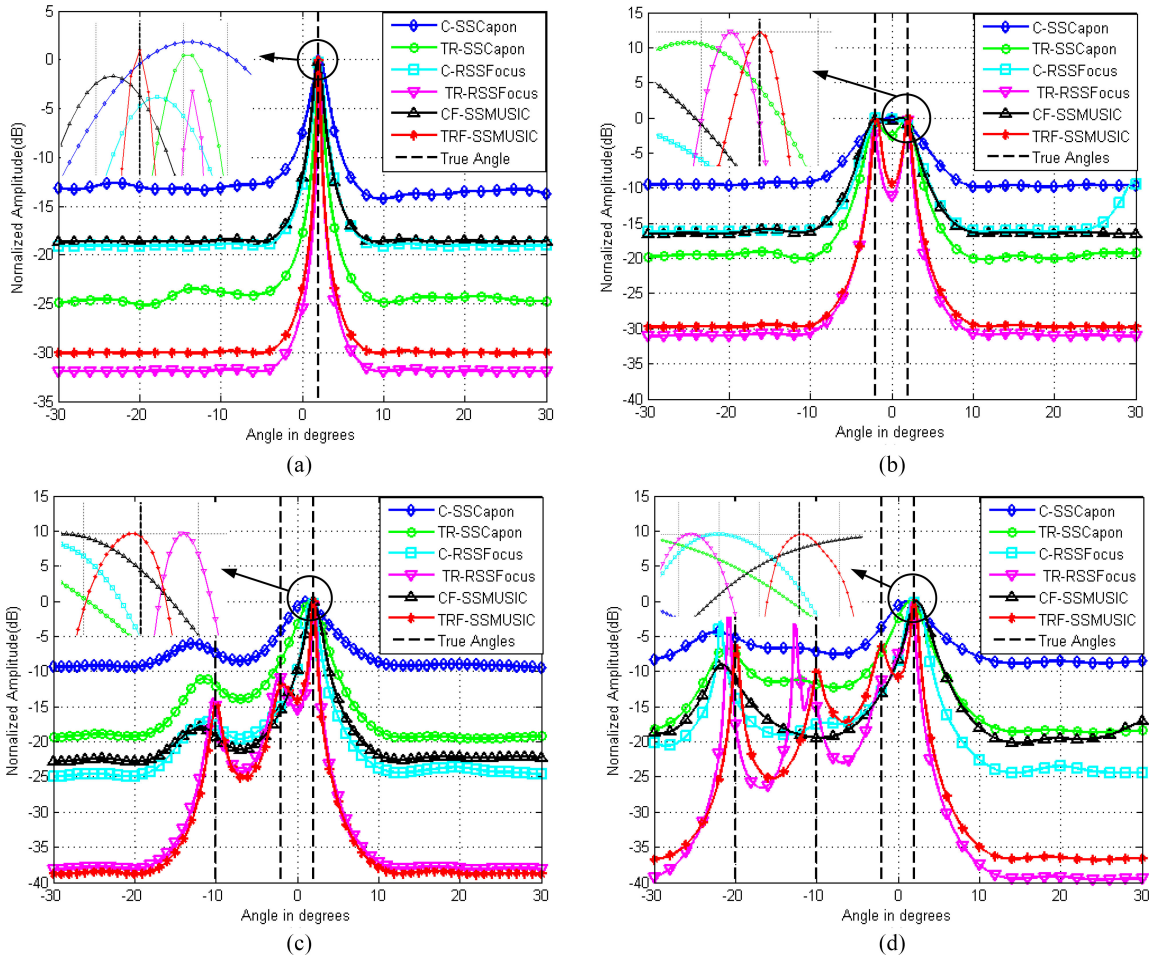


Fig. 10. Normalized spectra for the four different algorithms in different propagation models. (a) One-path model. (b) Two-path model. (c) Three-path model. (d) Four-path model.

C-RSSFocus, and TR-RSSFocus [41] algorithms described in Section I. First, we describe the parameters including angle range, time delay, and synthetic path attenuation factor in (1) and (4). Next, four experiments are conducted to verify the proposed algorithm from the following four aspects:

- 1) distribution of DOA estimation error of a target in multipath environment;
- 2) resolution capability;
- 3) root mean squares errors (RMSE) and statistical variance with respect to different SNRs based on Monte Carlo simulations;
- 4) RMSE versus different channel error factors also through Monte Carlo simulations.

#### A. Parameters Setup and Computation

We consider a representative low-angle scenario, where antenna altitude  $H_R = 10$  m, target altitude  $H_T = 10$  km, and the horizontal distance between the antenna and the target  $D = 300$  km. The fluctuation of the terrain is assumed to follow the Gaussian distribution with mean  $\mu = 0$  and variance  $\sigma = 1$  m. In this case, the corresponding angle range can be computed as shown in Table I. The time delay

of the direct path is given by

$$\tau_{\text{Direct}} = \frac{2 * \sqrt{D^2 + (H_T - H_R)^2}}{c} \approx 2 \text{ (ms)}. \quad (49)$$

Next, we consider the synthetic path attenuation factor  $X_P$ . From the antenna theory [44],  $X_P$  usually consists of three components including the smooth surface reflection coefficient  $\rho_1$ , the divergence factor  $\rho_D$ , and the surface roughness  $\rho_S$  [56]. We choose to model  $X_P = \rho_1 \rho_D \rho_S$  [57] and then calculate the corresponding  $X_P$  values as shown in Table II. Specific values of  $X_P$ ,  $\rho_1$ ,  $\rho_D$ ,  $\rho_S$  are depicted in Fig. 8 (also see [56], [57]).

#### B. Common Conditions for Simulations

We assume an ULA consisting of  $M = 16$  isotropic elements with an interelement sensor spacing  $d = \lambda_0/2$ ,  $\lambda_0 = c/f_c$  where  $f_c$  is the carrier frequency and  $c$  is the propagation speed of the probing signal. The probing signal is assumed to be a pulse with linear frequency modulation (LFM), i.e.,  $f(t) = \hat{f}(t)e^{j\omega_ct}$ , where the angular carrier frequency  $\omega_c = 2\pi f_c$ ,  $f_c = 200$  MHz. The complex envelope

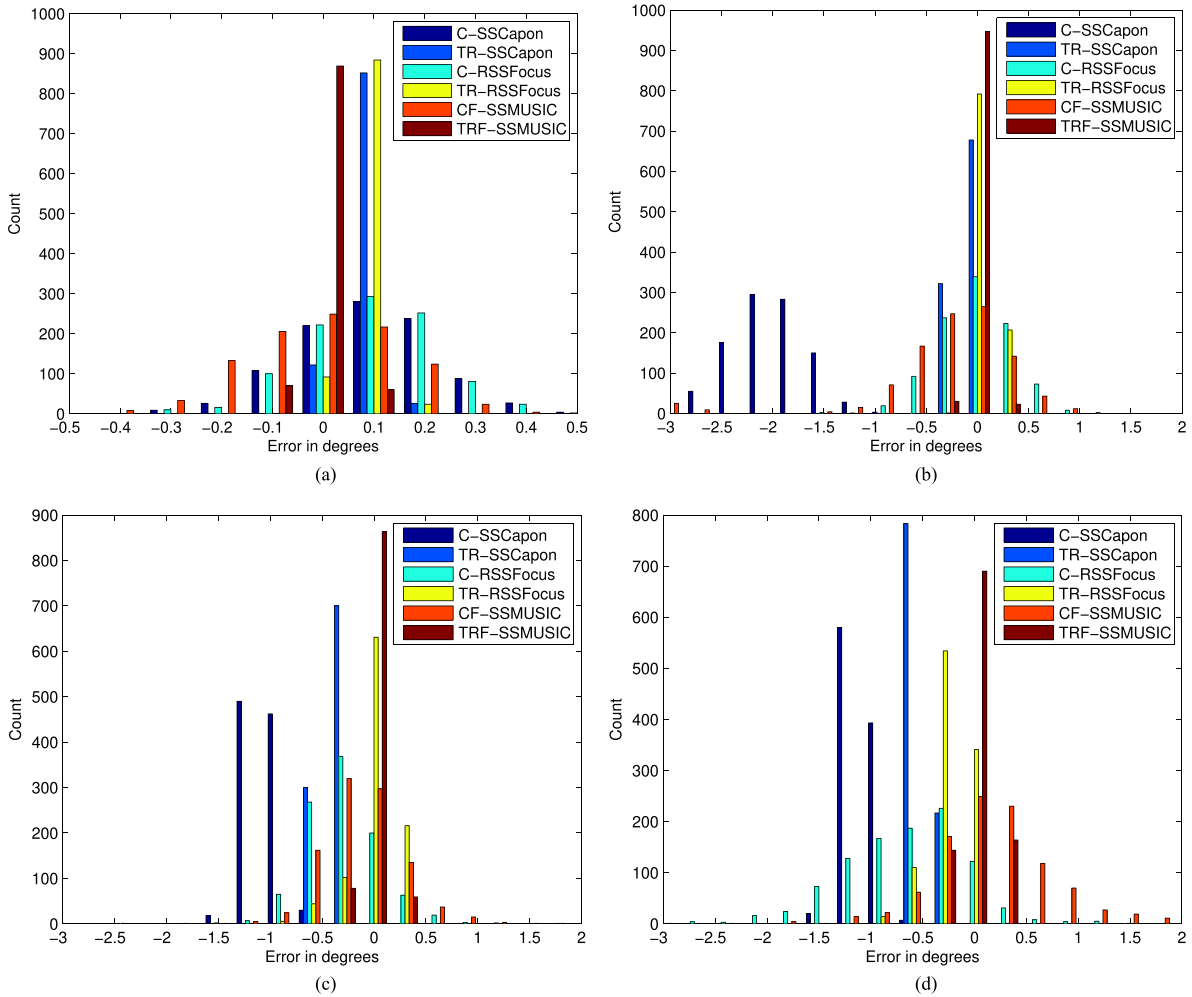


Fig. 11. Histograms showing the error distributions for the direct path angle at SNR = 5 dB in different propagation models. (a) One-path model. (b) Two-path model. (c) Three-path model. (d) Four-path model.

$\hat{f}(t)$  of the probing signal is

$$\hat{f}(t) = \frac{1}{\sqrt{\tau_0}} \text{Rect}\left(\frac{t}{\tau_0}\right) e^{j\pi\mu t^2} \quad (50)$$

where  $\text{Rect}\left(\frac{t}{\tau_0}\right) = 1, 0 \leq t < \tau_0$ . The bandwidth of  $f(t)$  is 20 MHz with carrier frequency 200 MHz. Fig. 9 shows the spectrum of the probing LFM signal used in this paper. The number of frequency bins  $Q$  is set to be 1000. Note that  $Q$  has to satisfy the sampling theorem in the frequency domain so as to maintain the integrity of the signal. To be more specific, we choose  $Q \geq \tau_0 \cdot B$  [50], which is a reasonable value for our one-path, two-path, three-path, and four-path propagation models to be discussed in the next section. Table II summarizes the corresponding parameters used in the signal model. We note that the time delays are computed with the direct path time delay given in (49) as the reference propagation delay.

### C. DOA Estimation Results and Error Distributions

The Monte Carlo simulation is based on the radar experimental setup shown in Fig. 5, where the corresponding

parameters are defined in Table II. SNRs are fixed at 5 dB for all 1-path, 2-path, 3-path, and 4-path propagation models. Note that, for all methods, the estimated DOAs are obtained as angle values of the  $P$  (the source number) largest peaks in the corresponding spectrum. For the easy of reference, we plot  $P$  vertical dashed lines to denote the true DOAs as shown in Fig. 10. Histograms of error distribution in 1-path, 2-path, 3-path, and 4-path propagation environments are depicted in Fig. 11. Table III lists the mean DOA estimation error of six different algorithms plotted in Fig. 11. By comprehensive analyses of Fig. 10, Fig. 11, and Table III, we reach the following conclusions.

- 1) In all of the four scenarios, the proposed TRF-SSMUSIC algorithm accurately estimates the DOAs of the target while the other five algorithms yield corresponding target location estimations with larger errors.
- 2) In all of the four 1-, 2-, 3-, and 4-path propagation cases shown in Fig. 11, the error spread of the TRF-SSMUSIC algorithm is more focused at  $0^\circ$ , which demonstrates the superiority of the proposed algorithm.
- 3) Fig. 11 indicates that both C-SSCapon and TR-SSCapon algorithms suffer from a systematic bias when the

TABLE III  
Mean DOA Estimation Error of Different Algorithms in Different Propagation Models

Path	Fig	DOA Method					
		C-SSCapon	TR-SSCapon	C-RSSFocus	TR-RSSFocus	CF-SSMUSIC	TRF-SSMUSIC
1	11.(a)	0.10°	0.09°	0.10°	0.09°	0.04°	0.01°
2	11.(b)	0.59°	0.18°	0.45°	0.12°	0.27°	0.06°
3	11.(c)	1.02°	0.40°	0.44°	0.17°	0.31°	0.08°
4	11.(d)	1.22°	0.46°	0.72°	0.26°	0.43°	0.12°

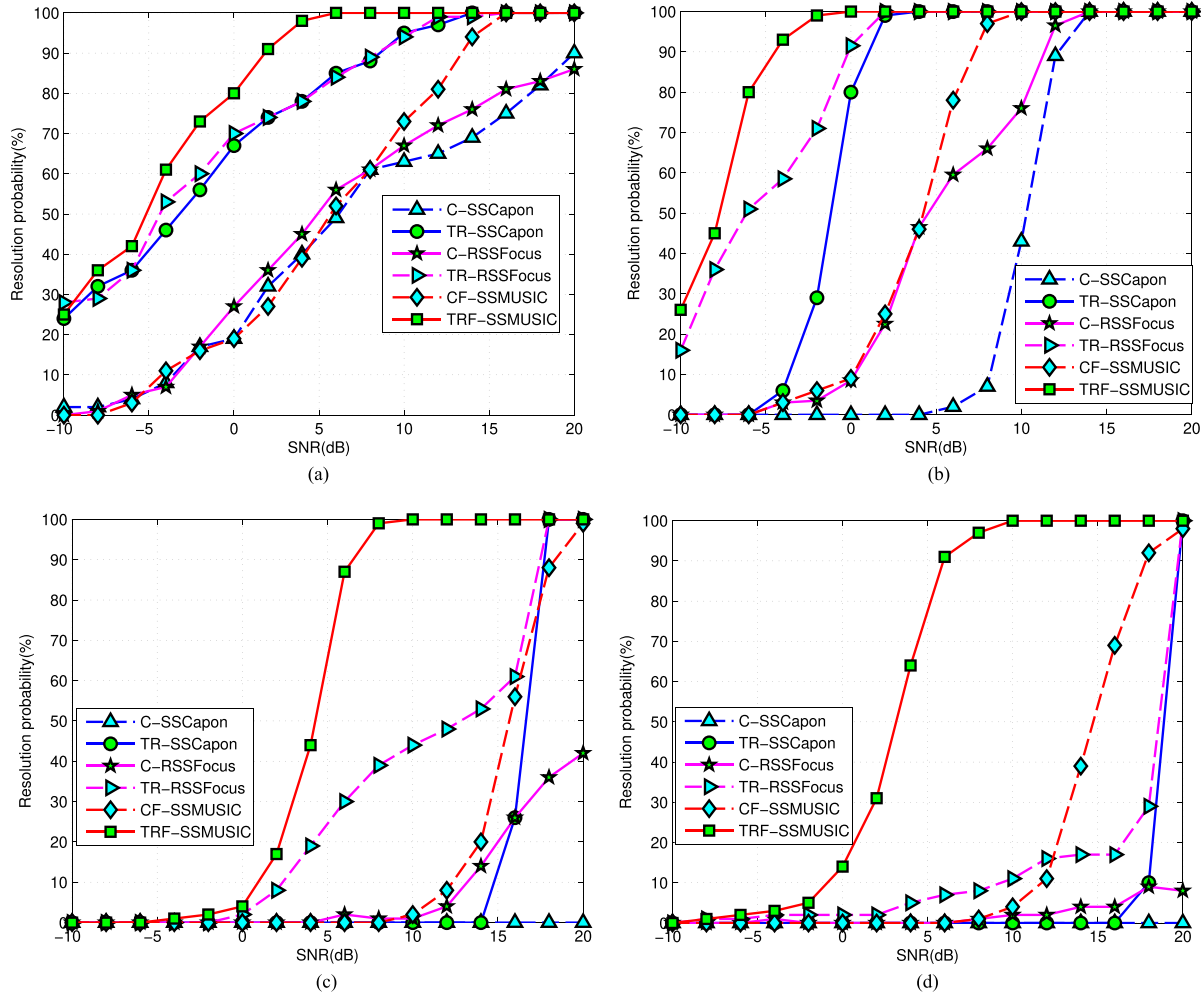


Fig. 12. Resolution probability of the four different algorithms in different propagation models. (a) 1-path model. (b) 2-path model.  
(c) 3-path model. (d) 4-path model.

number of sources is larger than one. The main reason is that the direct path and specular multipath signals appear to be two close symmetrical coherent sources. Thus, these two algorithms cannot resolve them successfully for a lack of resolution. In practice, they are more likely to treat them as a single source near their symmetrical center 0°, thus causing a systematic bias.

- 4) From Fig. 10, the performances of C-RSSFocus and TR-RSSFocus degrade significantly when  $P = 4$ , which results from their errors in the preliminary DOA estimations.

#### D. Resolution Probability Versus SNRs

In Fig. 12, we show the resolution performance of our TRF-SSMUSIC and other five benchmarking algorithms. Here, we take the resolution definition as in [40], i.e., if  $\mathbb{P}[(\theta_1 + \theta_2)/2] \leq [\mathbb{P}(\theta_1) + \mathbb{P}(\theta_2)]/2$ , then  $\theta_1$  and  $\theta_2$  are resolved successfully, where  $\theta_1$  and  $\theta_2$  represents two adjacent peaks in the pseudospectrum of corresponding algorithms. In particular, in 1-path scenario, if the error between the estimated DOA and the true DOA is less than 0.1°, we claim it is resolved successfully. This is because there is only one peak in this case where there is only one source, i.e.,  $P = 1$ . Evidently, Fig. 12 illustrates that our TRF-SSMUSIC has

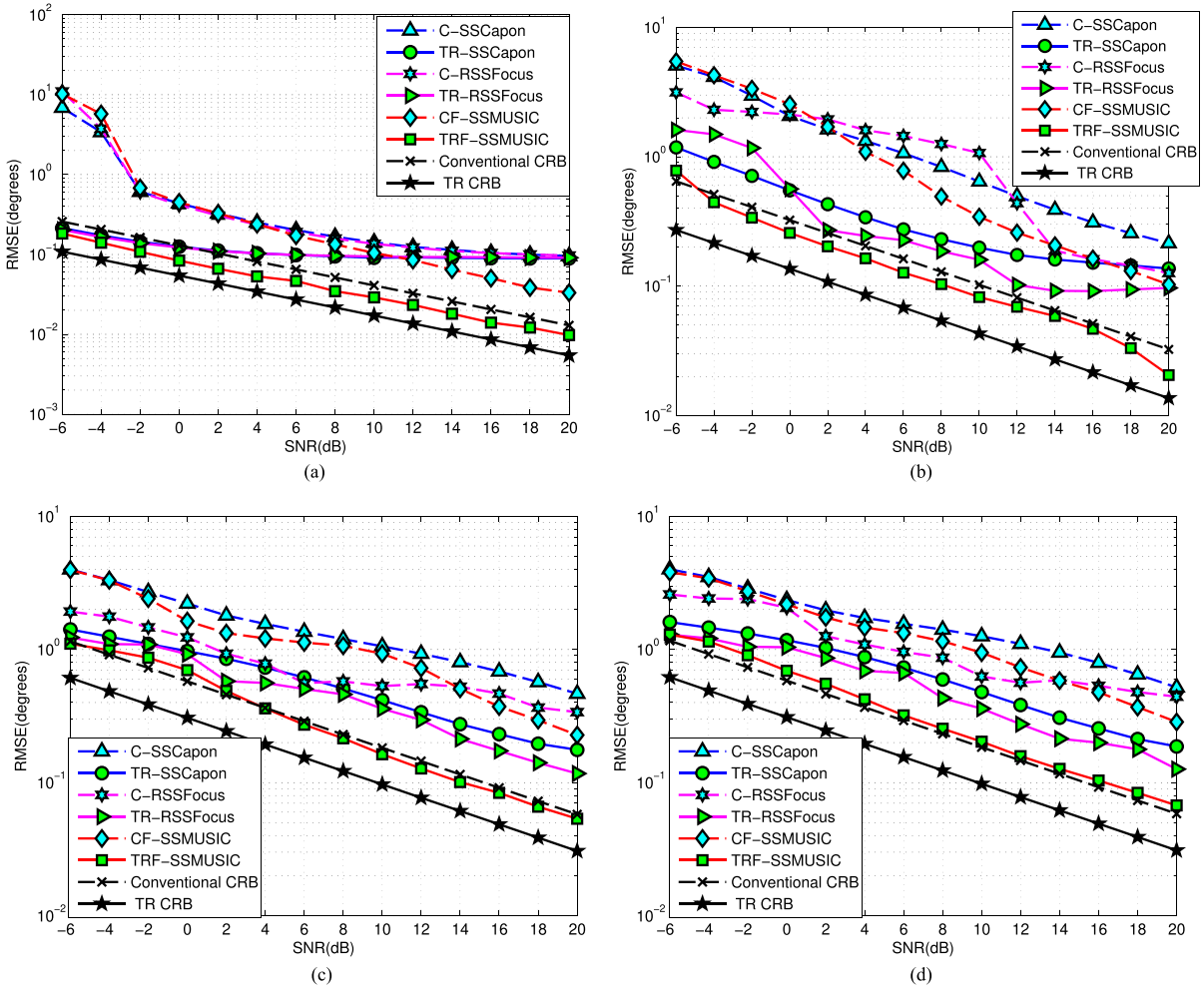


Fig. 13. Performance curves in terms of RMSE against SNR of four different propagation models. (a) 1-path model. (b) 2-path model. (c) 3-path model. (d) 4-path model.

better resolution performance than other five methods at low SNRs for all four scenarios. By comparing the results shown in Fig. 12(a)–(d), we observe that when the number of multipath signals increases, other five methods cannot accurately locate the targets even when SNR is as high as 10 dB. However, our TRF-SSMUSIC successfully estimates the DOA of the target even when source number increases to 4, as shown in Fig. 12(d). The performance improvement is benefited from the application of TR technique that garners the useful information contained in multipath signals.

#### E. RMSE and Statistical Variance Versus SNR

Fig. 13 shows the RMSE (in degrees) calculated from 1000 Monte Carlo trials for each SNR in all one-path, two-path, three-path, and four-path propagation models. Comparing the performance curves shown in Fig. 13, RMSE for our proposed TRF-SSMUSIC algorithm has the lowest values among all the algorithms, which implies that it improves the DOA precision in a certain degree. To be more specific, in the 2-path propagating case, setting the RMSE to  $0.5^\circ$ , we obtain the corresponding SNRs  $-5, 0, 0, 7, 10$ ,

and 12 dB for the six algorithms, respectively. We demonstrate that the TRF-SSMUSIC algorithm exhibits a better or the same RMSE value with lower SNR up to 5 dB; thus, verifying the superior performance of TRF-SSMUSIC algorithm in terms of RMSE and SNR compared with other five benchmark algorithms. Fig. 14 shows the statistical variances of all the six algorithms separately. The variances of corresponding conventional and TR-based algorithms in Fig. 14(a) are almost the same because there is no multipath distortion in this case (i.e.,  $P = 1$ ). However, when the number of multipath increases, as shown in Fig. 14(b)–(d), the TRF-SSMUSIC algorithm shows lower or comparable variance values than the other five methods. Hence, we conclude that our TRF-SSMUSIC algorithm demonstrates better robustness in different multipath scattering scenarios.

#### F. RMSE With Channel Errors

Finally, we present an example when there are channel errors (both in amplitude and phase). This is a practical problem that must be addressed in the TR method. As described in [58] and [59], we assume that the error factor  $\xi_m$  of the  $m$ th channel obeys a complex Gaussian distribution

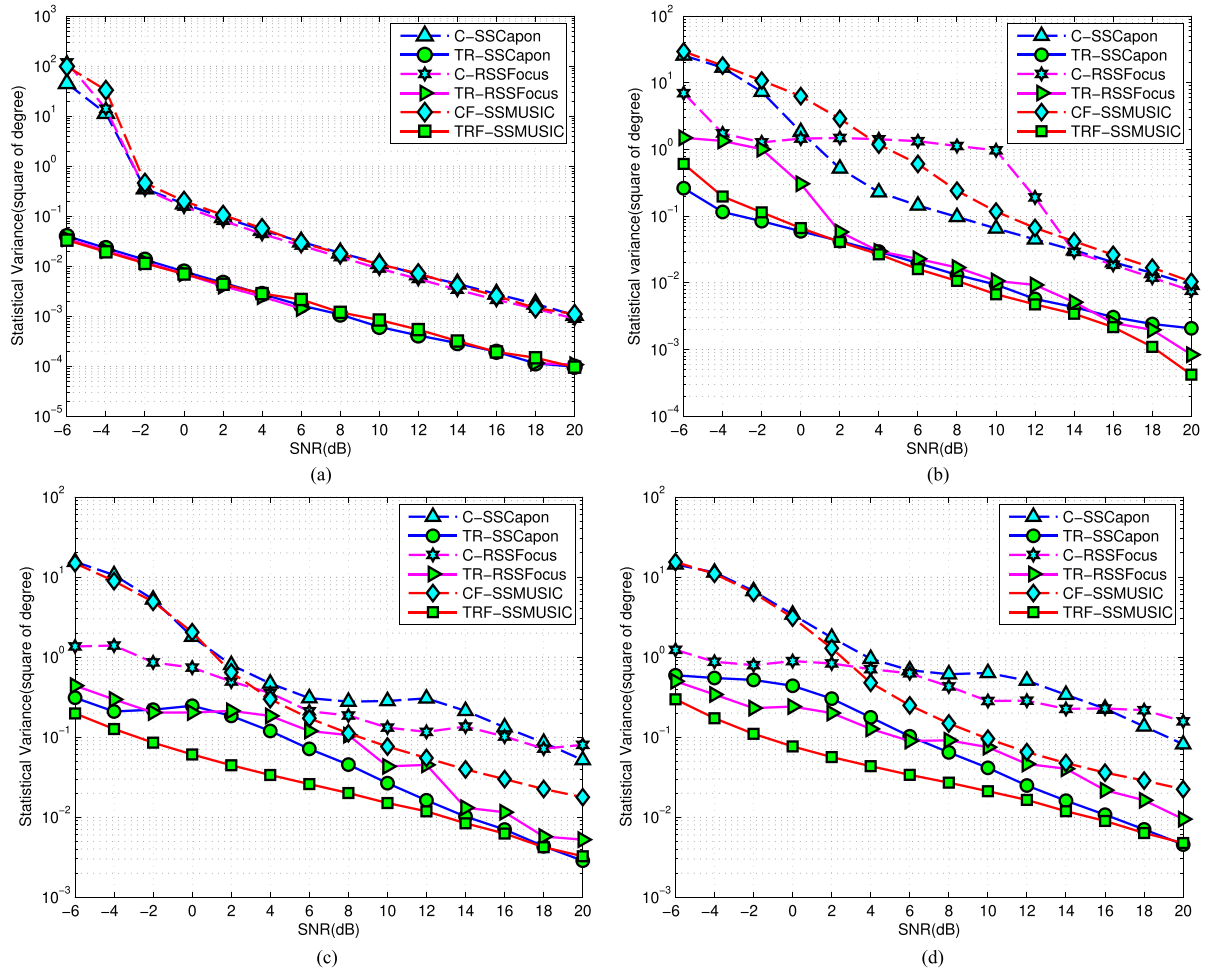


Fig. 14. Statistical variance curves versus SNR of four different propagation models. (a) 1-path model. (b) 2-path model. (c) 3-path model. (d) 4-path model.

with a zero mean and a variance  $\delta_F^2 e^{jw(\delta_F * \pi)^2}$ , that is

$$\xi_m \sim \mathcal{CN}\left(0, \delta_F^2 e^{jw(\delta_F * \pi)^2}\right) \quad (51)$$

where  $m = 1, 2, \dots, M$  and  $\delta_F$  is the error modulation factor distributing over  $[0, 1]$ . Let  $\boldsymbol{\xi} = [\xi_1, \xi_2, \dots, \xi_M]^T$  and take channel errors into consideration, forward-echo  $\mathbf{y}(\omega)$  and TR-Echo  $\mathbf{y}_{\text{TR}}(\omega)$ , given by (6) and (10), can be modified as follows, respectively:

$$\mathbf{y}(\omega) = \text{diag}[\boldsymbol{\xi}] \mathbf{A}(\Theta) \mathbf{X} \Gamma(\omega) \mathbf{F}(\omega) + \mathbf{v}(\omega) \quad (52)$$

$$\mathbf{y}_{\text{TR}}(\omega) = \mathbf{I}_M \otimes \text{diag}[\boldsymbol{\xi}] \mathbf{A}_{\text{TR}}(\Theta) \mathbf{X}_{\text{TR}} \Gamma_{\text{TR}}(\omega) \mathbf{Z}_{\text{TR}}(\omega) + \mathbf{n}(\omega). \quad (53)$$

Next, we test the proposed TRF-SSMUSIC algorithm and five benchmark CF-SSMUSIC, C-SSCapon, TR-SSCapon, C-RSSFocus, and TR-RSSFocus algorithms to perform DOA estimations. The results are presented in Fig. 15.

Note that SNR is fixed at 5 dB and  $\delta_F = 0$  means that there is no channel error. Fig. 15 shows that the DOA estimation performance degrades with the increasing value of  $\delta_F$ , which is consistent with the practical scenarios described in [58] and [59]. Specifically, the enhancement of DOA estimation performance by taking the TR depends on

whether the TR probing signal can refocus at the exact position of the target. Moreover, deviation from the reciprocity condition will result in channel mismatch, which will affect the refocusing process, thus, degrading the final DOA estimation performance. Nevertheless, our results show that the RMSE of our proposed TRF-SSMUSIC algorithm is lower than the other five benchmark algorithms in all of the four 1-path, 2-path, 3-path and 4-path channel environments. Therefore, it shows clearly that the TRF-SSMUSIC algorithm proposed in this paper is more robust and viable in real-word scenarios.

#### G. Computational Complexity Analysis

In this subsection, we analyze the computational complexity of our proposed TRF-SSMUSIC algorithm and compare it with other five benchmark algorithms. As denoted before,  $M$  is the number of elements in array A,  $Q$  is the number of frequency bins, and  $P$  is the number of sources. Note that we use single complex multiplication (CM) [60] as the statistical unit. The computational complexity can be analyzed by the following steps.

- 1) Executing fast Fourier transform to obtain corresponding frequency model needs  $M[\frac{N}{2} \log_2(N)]$  CMs, where

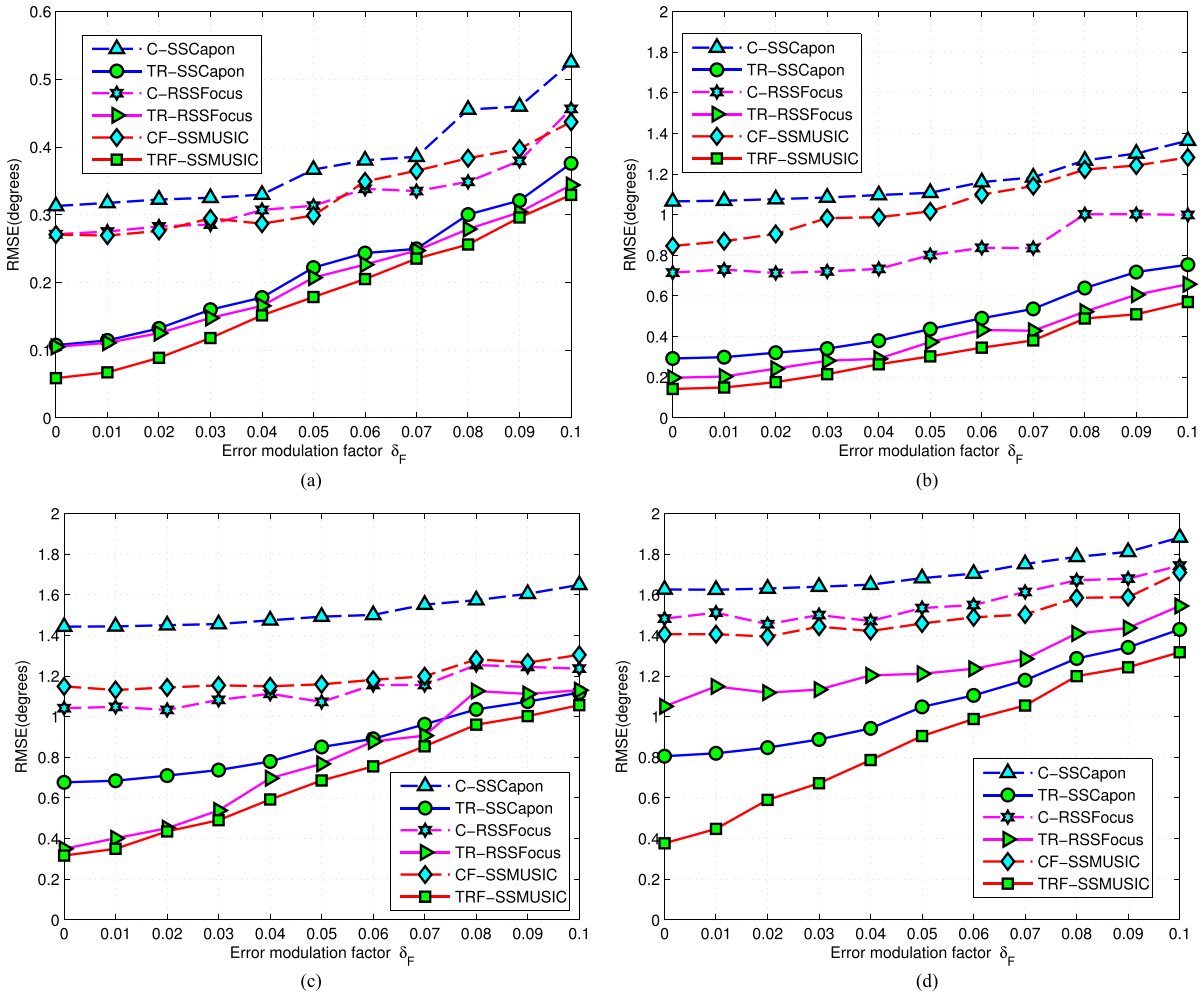


Fig. 15. Performance curves in terms of RMSE against error modulation factors  $\delta_F$  in four different propagation models. (a) 1-path model. (b) 2-path model. (c) 3-path model. (d) 4-path model.

TABLE IV  
Computational Complexity Comparisons

Algorithms	Computational complexity	Simulations (CMs)
C-SSCapon	$O\{M[\frac{N}{2}\log_2(N)] + Q(M^3 + M^2) + JQ(M^2 + M)\}$	$1.637 \times 10^9$
TR-SSCapon	$O\{3M[\frac{N}{2}\log_2(N)] + 4MN + Q(M^3 + M^2) + JQ(M^2 + M)\}$	$1.638 \times 10^9$
C-RSSFocus	$O\{M[\frac{N}{2}\log_2(N)] + 3QM^3 + (2QP + 14J)M^2 + [2J(M - P) + 101J - P + 1]M\}$	$4.801 \times 10^7$
TR-RSSFocus	$O\{3M[\frac{N}{2}\log_2(N)] + 4MN + 3QM^3 + (2QP + 14J)M^2 + [2J(M - P) + 101J - P + 1]M\}$	$4.931 \times 10^7$
CF-SSMUSIC	$O\{M[\frac{N}{2}\log_2(N)] + Q(5M^3 + M^2) + JM[2(M - P) + 1]\}$	$2.382 \times 10^7$
TRF-SSMUSIC	$O\{3M[\frac{N}{2}\log_2(N)] + 4MN + Q(5M^3 + M^2) + JM[2(M - P) + 1]\}$	$2.480 \times 10^7$

$N$  is the number of snapshots in time domain as denoted in (1).

- 2) TR process including phase conjugation and energy normalization in the frequency domain takes  $O(4MN)$  CMs.
- 3) Computing the covariance matrix  $\mathfrak{R}_y^{\text{TR}}(\omega_q)$  in (12) needs  $O(QM^2)$  CMs.

- 4) Computing the transform matrix  $\mathbf{T}_q(\omega_q)$  in (16) which includes eigenvalue decomposition and SVD takes  $O(2QM^3)$  CMs.
- 5) Computing the focusing covariance matrix  $\mathfrak{R}_y^{\text{TR}}(0)$  in (23) takes  $O(2QM^3)$  CMs.
- 6) Performing DOA estimation  $\mathbb{P}_{\text{TR}}(\theta)$  in (24) needs  $O\{M[2(M - P) + 1] \cdot J\}$  CMs, where  $J$  denotes the

angle grid number, i.e.,  $\{\theta_b\}_{j=1}^J$  covers the all the possible directions of  $\theta$ .

The analysis of computational complexities of the six algorithms is summarized in Table IV. We also include a specific example where the array element number  $M = 16$ , the frequency bin  $Q = 1000$ , and the angle grid number  $J$  is 6000 to cover the angle of interest, i.e.,  $-30^\circ \sim 30^\circ$ . We conclude that our TRF-SSMUSIC algorithm reduces the computational cost significantly compared with the C-SSCapon and TR-SSCapon in [8], which uses the ISM method for wideband signals. That is mainly because the ISM method performs DOA estimation for every frequency bin; thus, increasing the computational complexity rapidly when  $Q$  is rather large. Compared with C-RSSFocus and TR-RSSFocus, the TRF-SSMUSIC algorithm has a lower computational load because there is no need for preliminary DOA estimation.

## VI. CONCLUSION

In this paper, we develop a novel algorithm to estimate DOAs for low-angle targets in a rich multipath environment by utilizing the TR method. We develop a signal model by analyzing the angle ranges of multipath signals of a low-angle target in complex terrain. The proposed algorithm combines the TR and the signal subspace method-CSM to solve the DOA estimation problem in wideband. We also derive the theoretical CRB for the proposed TRF-SSMUSIC algorithm and compare it with other five algorithms for DOA estimation. We show that matching the transmitted signal to the multipath propagation channel by TR improves the DOA estimation accuracy. Furthermore, the signal subspace method enables accurate localization of closely separated coherent sources in wideband signals. By simulations, we show that the proposed algorithm exploits rich multipath to its advantage and outperforms other conventional algorithms in terms of estimation accuracy and resolution. Our method also shows robustness against complex channel errors and other interferences, such as slow motion of the target, channel mismatch, and other additive channel noise. We note that the validation of the reciprocity of the propagation environment in complex terrain may be limited to some extent in practice. Thus, further compensation techniques to the TR focusing property due to the loss of reciprocity for DOA estimation in real-world scenarios are still open research problems and will be addressed in a companion paper.

## APPENDIX A

In this appendix, we prove the rationality of the approximation in (4). First, we note that our entire proof is based on a typical low-angle scenario used in our simulations, in which Section V-A describes a working environment and Section V-B defines the probing signal parameters of a common VHF radar system aiming at low-angle target detection and localization. We prove that the assumption about target velocity  $v \leq 900$  m/s is reasonable in our TR-based signal model.

Assume that the relative bandwidth of the probing signal is 0.1 (i.e.,  $B = 0.1 * \omega_c$ ), according to (50). As noted in (3) and (4),  $F(\omega)$  is the spectrum of LFM probing signal  $f(t)$ , which has a rectangle shape with bandwidth  $B$ . Then, shifting  $F(\omega)$  by  $\omega_p$  yields  $F(\omega + \omega_p)$ . Note that in Section III, the spectrum of TR setup observation vector  $\mathbf{y}_{\text{TR}}(\omega)$  is divided into  $Q$  equally spaced frequency bins. Then, the CSM method is utilized to deal with the wideband received signals  $\mathbf{y}_{\text{TR}}(\omega)$ . In other words, if the shift value  $\omega_p$  is much smaller than the sample interval (i.e.,  $|\omega_q - \omega_{q-1}|$ ), the shift from  $F(\omega)$  to  $F(\omega + \omega_p)$  will not affect the sample results about  $\mathbf{y}_{\text{TR}}(\omega)$ . Thus, the ultimate DOA estimation result will not be affected.

Next, the problem turns into proving that the Doppler frequency component  $\omega_p$  caused by the velocity of the target is much smaller than sample interval. We assume that

$$\omega_p = \omega_c \beta_p = \omega_c v_p / c \leq 3\% * B / Q \iff \omega_p \ll B / Q \quad (54)$$

where  $\iff$  means equivalence in derivation. Given the parameters in (50), we calculate the target velocity  $v_p$  based on (54) by

$$v_p \leq \frac{3\% * B * c}{\omega_c * Q} = 900 \text{ (m/s)}. \quad (55)$$

Equation (55) is one of the constraint conditions about  $v_p$ . On the other hand, we noted before that the TR involves a second probing of the target by resending the TR signal, which means that the target displacement between the entire process cannot be larger than one range resolution unit  $\Delta_R$ , that is,  $\Delta_R = c/(2 * B) = 7.5$  m. As noted in (49), the propagation time of the direct path wave  $\tau_{\text{Direct}}$  is 2 ms. We assume the TR process in the antenna array is sufficiently small, thus, the target displacement  $\Delta_S$  between the entire probing process can be computed as  $\Delta_S \leq v * 2 * \tau_{\text{Direct}} = 3.6$  m, which is smaller than the size of majority of low-angle targets, such as aircrafts and missiles. Furthermore,  $\Delta_S < \Delta_R$  means that the target is within the same range unit in the entire probing process. Therefore, we prove that the TR probing signal can refocus at the target position, which is important in TR-based localization algorithms. Hence, we conclude that  $v \leq 900$  m/s is a reasonable assumption, thus, making the approximation in (4) valid.

## APPENDIX B

In this appendix, we prove (14) and (16) by citing the following Lemma and a Corollary [61] for the sake of completeness.

**LEMMA A** Let  $\mathbf{A}, \mathbf{B} \in \mathbf{M}_{m \times n}$  (a  $m \times n$  matrix), and  $q = \min\{m, n\}$ .  $\sigma_i(\mathbf{A}), \sigma_i(\mathbf{B}), \sigma_i(\mathbf{AB}^H), i = 1, 2, \dots, q$ , respectively, denote the nonzero singular values of the corresponding matrices arranged in nonincreasing order. Then, for unitary matrix  $\mathbf{U} \in \mathbf{M}_{m \times m}$ ,  $\mathbf{V} \in \mathbf{M}_{n \times n}$

$$\max_{\mathbf{U}, \mathbf{V}} \{\text{Re} [\text{tr}(\mathbf{AV}^H \mathbf{B}^H \mathbf{U}^H)]\} = \sum_{i=1}^q \sigma_i(\mathbf{A}) \sigma_i(\mathbf{B}). \quad (56)$$

**COROLLARY A** If  $\mathbf{A}$  is a square Hermitian matrix,  $\mathbf{P}$  is the eigenmatrix constructed by eigenvectors of  $\mathbf{A}$ , then  $\mathbf{P}$  is

a unitary matrix and  $\mathbf{A} = \mathbf{P}\Lambda\mathbf{P}^H$

$$\Lambda = \begin{bmatrix} \lambda_1 & & & \\ & \lambda_2 & & \\ & & \ddots & \\ & & & \lambda_n \end{bmatrix} \quad (57)$$

where  $\lambda_1, \dots, \lambda_n$  are the  $n$  unique eigenvalues of matrix  $\mathbf{A}$ .

We use Lemma A and Corollary A to prove (14) and (16). Note that

$$\|\mathbf{A} - \mathbf{U}\mathbf{B}\mathbf{V}^H\|_F^2 = \|\mathbf{A}\|_F^2 + \|\mathbf{B}\|_F^2 - 2\operatorname{Re}[\operatorname{tr}(\mathbf{A}\mathbf{B}\mathbf{V}^H\mathbf{U}^H)]. \quad (58)$$

Minimization of (58) with respect to the choice of  $\mathbf{U}$  and  $\mathbf{V}$  is equivalent to maximizing  $\operatorname{Re}[\operatorname{tr}(\mathbf{A}\mathbf{B}\mathbf{V}^H\mathbf{U}^H)]$ , i.e.,

$$\mathbf{U}, \mathbf{V} = \arg \max_{\mathbf{U}, \mathbf{V}} \{\operatorname{Re}[\operatorname{tr}(\mathbf{A}\mathbf{B}\mathbf{V}^H\mathbf{U}^H)]\}. \quad (59)$$

From Lemma A, we see that the maximum value of (59) is given by  $\sum_{i=1}^q \sigma_i(\mathbf{A})\sigma_i(\mathbf{B})$ . Let the SVD of the two matrices  $\mathbf{A}$  and  $\mathbf{B}$  be

$$\mathbf{A} = \mathbf{E}\Lambda_{\mathbf{A}}\mathbf{F}^H, \mathbf{B} = \mathbf{X}\Lambda_{\mathbf{B}}\mathbf{Y}^H \quad (60)$$

where  $\mathbf{E}, \mathbf{F}, \mathbf{X}, \mathbf{Y}$  are the corresponding singular matrix. The maximum of (59) is given by the multiplication of the singular values of the diagonal matrices  $\Lambda_{\mathbf{A}}$  and  $\Lambda_{\mathbf{B}}$ . Suppose

$$\mathbf{U} = \mathbf{E}\mathbf{X}^H, \mathbf{V} = \mathbf{F}\mathbf{Y}^H \quad (61)$$

then

$$\mathbf{A}\mathbf{B}\mathbf{V}^H\mathbf{U}^H = \mathbf{E}\Lambda_{\mathbf{A}}\mathbf{F}^H\mathbf{F}\mathbf{Y}^H\mathbf{Y}\Lambda_{\mathbf{B}}\mathbf{X}^H\mathbf{X}\mathbf{E}^H = \mathbf{E}\Lambda_{\mathbf{A}}\Lambda_{\mathbf{B}}\mathbf{E}^H \quad (62)$$

where  $\mathbf{E}^H\mathbf{E} = \mathbf{I}$ ,  $\mathbf{X}^H\mathbf{X} = \mathbf{I}$ ,  $\mathbf{F}^H\mathbf{F} = \mathbf{I}$ ,  $\mathbf{Y}^H\mathbf{Y} = \mathbf{I}$ .

From (57) and (62), we obtain

$$\begin{aligned} \operatorname{Re}[\operatorname{tr}(\mathbf{A}\mathbf{B}\mathbf{V}^H\mathbf{U}^H)] &= \operatorname{Re}[\operatorname{tr}(\mathbf{E}\Lambda_{\mathbf{A}}\Lambda_{\mathbf{B}}\mathbf{E}^H)] \\ &= \operatorname{tr}(\Lambda_{\mathbf{A}}\Lambda_{\mathbf{B}}) = \sum_{i=1}^q \sigma_i(\mathbf{A})\sigma_i(\mathbf{B}). \end{aligned} \quad (63)$$

Evidently, (61) is the solution to (59), based on (62) and (63). Next, we consider a special case where  $\mathbf{A}$  and  $\mathbf{B}$  are square Hermitian matrices. Using Corollary A, we obtain

$$\mathbf{A} = \mathbf{P}\Lambda_{\mathbf{A}}\mathbf{P}^H, \mathbf{B} = \mathbf{K}\Lambda_{\mathbf{B}}\mathbf{K}^H. \quad (64)$$

From (61), we obtain

$$\mathbf{U} = \mathbf{V} = \mathbf{PK}^H \quad (65)$$

where  $\mathbf{P}$  and  $\mathbf{K}$  are eigenmatrices constructed by the eigenvectors of  $\mathbf{A}$  and  $\mathbf{B}$ , respectively. From Lemma A and (63), if  $\mathbf{U}$  and  $\mathbf{V}$  satisfy (61), they are the solution of (59). As we have pointed out after (58), the solution of (59) minimizes (58) equivalently. Thus, we conclude (61) is the solution to the following equation:

$$\arg \min_{\mathbf{U}, \mathbf{V}} \|\mathbf{A} - \mathbf{U}\mathbf{B}\mathbf{V}^H\|_F^2. \quad (66)$$

Furthermore, if  $\mathbf{A}$  and  $\mathbf{B}$  are square Hermitian matrices, from (64) and (65), the solution of (66) is simplified as (65).

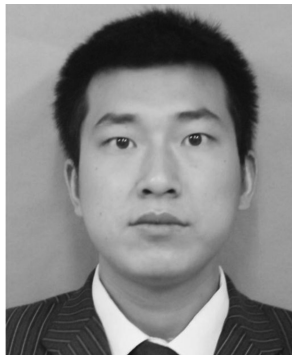
By recalling (14),  $\mathfrak{R}_y^{\text{TR}}(\omega_0)$  and  $\mathfrak{R}_y^{\text{TR}}(\omega_q)$  are both Hermitian matrices because they are the covariance matrices of the observed signals at corresponding frequency bin. Comparing (14) and (66), we can show that the solution of (14) is  $\mathbf{T}_q(\omega_q) = \mathbf{U}(\omega_0)\mathbf{U}^H(\omega_q)$ , where  $\mathbf{U}(\omega_0)$  and  $\mathbf{U}(\omega_q)$  denote the eigenmatrices constructed by eigenvectors of  $\mathfrak{R}_y^{\text{TR}}(\omega_0)$  and  $\mathfrak{R}_y^{\text{TR}}(\omega_q)$ , respectively. The proof of (14) and (16) is completed.

## REFERENCES

- [1] Z. Xu, Z. Xiong, J. Wu, and S. Xiao  
Symmetrical difference pattern monopulse for low-angle tracking with array radar  
*IEEE Trans. Aerosp. Electron. Syst.*, vol. 52, no. 6, pp. 2676–2684, Dec. 2016.
- [2] D. Park, E. Yang, S. Ahn, and J. Chun  
Adaptive beamforming for low-angle target tracking under multipath interference  
*IEEE Trans. Aerosp. Electron. Syst.*, vol. 50, no. 4, pp. 2564–2577, Oct. 2014.
- [3] B. Chen, G. Zhao, and S. Zhang  
Altitude measurement based on beam split and frequency diversity in VHF radar  
*IEEE Trans. Aerosp. Electron. Syst.*, vol. 46, no. 1, pp. 3–13, Jan. 2010.
- [4] U. Kumbul and H. T. Hayvaci  
Knowledge-aided adaptive detection with multipath exploitation radar  
in *Proc. Sensor Signal Process. Defence*, Sep. 2016, pp. 1–4.
- [5] W. Zhu and B. X. Chen  
Altitude measurement based on terrain matching in VHF array radar  
*Circuits Syst. Signal Process.*, vol. 32, no. 2, pp. 647–662, Apr. 2013.
- [6] S. Wang, Y. Cao, H. Su, and Y. Wang  
Target and reflecting surface height joint estimation in low-angle radar  
*IET Radar, Sonar Navig.*, vol. 10, no. 3, pp. 617–623, Feb. 2016.
- [7] M. A. Sebt, A. Sheikhi, and M. M. Nayebi  
Robust low-angle estimation by an array radar  
*IET Radar, Sonar Navig.*, vol. 4, no. 6, pp. 780–790, Dec. 2010.
- [8] F. Foroozan and A. Asif  
Time reversal based active array source localization  
*IEEE Trans. Signal Process.*, vol. 59, no. 6, pp. 2655–2668, Jun. 2011.
- [9] S. N. K. Chithra, and T. Sudhakar  
Performance analysis of linear recursive least squares adaptive filter to mitigate multipath effect  
in *Proc. Int. Symp. Ocean Electron.*, Nov. 2015, pp. 1–6.
- [10] H. Naseri and V. Koivunen  
Cooperative simultaneous localization and mapping by exploiting multipath propagation  
*IEEE Trans. Signal Process.*, vol. 65, no. 1, pp. 200–211, Jan. 2017.
- [11] M. Fink, G. Montaldo, and M. Tanter  
Time reversal acoustics  
in *Proc. IEEE Ultrason. Symp.*, Aug. 2004, vol. 2, pp. 850–859.
- [12] H. C. Song, W. A. Kuperman, W. S. Hodgkiss, T. Akal, and C. Ferla  
Iterative time reversal in the ocean  
*J. Acoust. Soc. Amer.*, vol. 105, no. 6, pp. 3176–3184, May 1999.

- [13] M. Fink and C. Prada  
Acoustic time-reversal mirrors  
*Inverse Problems*, vol. 17, no. 1, pp. R1–R38, 2001.
- [14] F. Foroozan and P. Sadeghi  
Super-resolution ultrawideband ultrasound imaging using focused frequency time reversal MUSIC  
in *Proc. IEEE Int. Conf. Acoust., Speech Signal Process.*, Apr. 2015, pp. 887–891.
- [15] K. J. R. Liu, B. Wang, Y. Han, H. Q. Lai, and Z. Safar  
Why time reversal for future 5G wireless?  
*IEEE Signal Process. Mag.*, vol. 33, no. 2, pp. 17–26, Mar. 2016.
- [16] Z. Wang, J. Li, and R. Wu  
Time-delay and time-reversal-based robust capon beamformers for ultrasound imaging  
*IEEE Trans. Med. Imag.*, vol. 24, no. 10, pp. 1308–1322, Oct. 2005.
- [17] A. J. Devaney  
Time reversal imaging of obscured targets from multistatic data  
*IEEE Trans. Antennas Propag.*, vol. 53, no. 5, pp. 1600–1610, May 2005.
- [18] Y. Jin and J. M. F. Moura  
Time-reversal detection using antenna arrays  
*IEEE Trans. Signal Process.*, vol. 57, no. 4, pp. 1396–1414, Apr. 2009.
- [19] N. O’Donoughue and J. M. F. Moura  
Gaussian target detection in multipath clutter with single-antenna time reversal  
*IEEE Trans. Signal Process.*, vol. 61, no. 15, pp. 3733–3744, Aug. 2013.
- [20] F. Foroozan, A. Asif, and Y. Jin  
Cramer-Rao bounds for time reversal MIMO radars with multipath  
*IEEE Trans. Aerosp. Electron. Syst.*, vol. 52, no. 1, pp. 137–154, Feb. 2016.
- [21] Y. Jin, J. M. F. Moura, and N. O’Donoughue  
Time reversal in multiple-input multiple-output radar  
*IEEE J. Sel. Topics Signal Process.*, vol. 4, no. 1, pp. 210–225, Feb. 2010.
- [22] Y. Jin, J. M. F. Moura, Y. Jiang, D. Stancil, and N. O’Donoughue  
Time reversal target classification from scattered radiation  
in *Proc. IEEE 14th Workshop Statist. Signal Process.*, Aug. 2007, pp. 317–321.
- [23] F. Foroozan and A. Asif  
Time reversal: Algorithms for M-array target classification using array signal processing  
in *Proc. IEEE Mil. Commun. Conf.*, Jun. 2008, pp. 1–7.
- [24] F. Foroozan and A. Asif  
Effect of multipaths on N-ary time reversal classifiers  
in *Proc. IEEE Int. Symp. Signal Process. Inf. Technol.*, Dec. 2008, pp. 309–314.
- [25] X. Zeng, M. Yang, B. Chen, and Y. Jin  
Low angle direction of arrival estimation by time reversal  
in *Proc. 2017 Int. Conf. Acoust., Speech Signal Process.*, Mar. 2017, pp. 3161–3165.
- [26] R. Schmidt  
Multiple emitter location and signal parameter estimation  
*IEEE Trans. Antennas Propag.*, vol. 34, no. 3, pp. 276–280, Mar. 1986.
- [27] M. Kaveh and A. Barabell  
The statistical performance of the MUSIC and the minimum-norm algorithms in resolving plane waves in noise  
*IEEE Trans. Acoust., Speech, Signal Process.*, vol. 34, no. 2, pp. 331–334, Apr. 1986.
- [28] B. Friedlander  
A sensitivity analysis of the MUSIC algorithm  
*IEEE Trans. Acoust., Speech, Signal Process.*, vol. 38, no. 10, pp. 1740–1751, Oct. 1990.
- [29] M. E. Yavuz and F. L. Teixeira  
Space-frequency ultrawideband time reversal imaging  
*IEEE Trans. Geosci. Remote Sensing*, vol. 46, no. 4, pp. 1115–1124, Apr. 2008.
- [30] D. Ciunzo, G. Romano, and R. Solimene  
Performance analysis of time-reversal MUSIC  
*IEEE Trans. Signal Process.*, vol. 63, no. 10, pp. 2650–2662, May 2015.
- [31] C. Domenico and R. P. Salvo  
Noncolocated time-reversal MUSIC: High-SNR distribution of null spectrum  
*IEEE Signal Process. Lett.*, vol. 24, no. 4, pp. 397–401, Jan. 2017.
- [32] L. Yassin and L. Huang  
TR-MUSIC inversion of the density and compressibility contrasts of point scatterers  
*IEEE Trans. Ultrason., Ferroelect., Freq. Control*, vol. 61, no. 1, pp. 16–24, Jan. 2014.
- [33] H. Wang and M. Kaveh  
Coherent signal-subspace processing for the detection and estimation of angles of arrival of multiple wide-band sources  
*IEEE Trans. Acoust., Speech, Signal Process.*, vol. 33, no. 4, pp. 823–831, Aug. 1985.
- [34] S. Valaee, B. Champagne, and P. Kabal  
Localization of wideband signals using least-squares and total least-squares approaches  
*IEEE Trans. Signal Process.*, vol. 47, no. 5, pp. 1213–1222, May 1999.
- [35] M. R. Azimi-Sadjadi, A. Pezeshki, and N. Rosevare  
Wideband DOA estimation algorithms for multiple moving sources using unattended acoustic sensors  
*IEEE Trans. Aerosp. Electron. Syst.*, vol. 44, no. 4, pp. 1585–1599, Oct. 2008.
- [36] M. Wax, T. J. Shan, and T. Kailath  
Spatio-temporal spectral analysis by eigenstructure methods  
*IEEE Trans. Acoust., Speech, Signal Process.*, vol. 32, no. 4, pp. 817–827, Aug. 1984.
- [37] G. Zhao and G. Shi  
Altitude measurement of low elevation target based on iterative subspace projection  
*IEEE Trans. Aerosp. Electron. Syst.*, vol. 47, no. 2, pp. 1256–1264, Apr. 2011.
- [38] T. Shan, M. Wax, and T. Kailath  
On spatial smoothing for direction-of-arrival estimation of coherent signals  
*IEEE Trans. Acoust., Speech, Signal Process.*, vol. 33, no. 4, pp. 806–811, Aug. 1985.
- [39] S. Valaee and P. Kabal  
Wideband array processing using a two-sided correlation transformation  
*IEEE Trans. Signal Process.*, vol. 43, no. 1, pp. 160–172, Jan. 1995.
- [40] Y. Wang and H. Chen  
*Spectra Estimation Theory and Algorithm*. Beijing, China: Tsinghua Univ. Press, 2009.
- [41] H. Hung and M. Kaveh  
Focussing matrices for coherent signal-subspace processing  
*IEEE Trans. Acoust., Speech, Signal Process.*, vol. 36, no. 8, pp. 1272–1281, Aug. 1988.
- [42] M. A. Doron and A. J. Weiss  
On focusing matrices for wide-band array processing  
*IEEE Trans. Signal Process.*, vol. 40, no. 6, pp. 1295–1302, Jun. 1992.
- [43] J. Li, P. Stoica, and Z. Wang  
On robust Capon beamforming and diagonal loading  
*IEEE Trans. Signal Process.*, vol. 51, no. 7, pp. 1702–1715, Jul. 2003.

- [44] W. Croswell  
*Antenna Theory, Analysis, and Design*. New York, NY, USA: Harper and Row, 1982.
- [45] D. B. Williams and D. H. Johnson  
Using the sphericity test for source detection with narrow-band passive arrays  
*IEEE Trans. Acoust., Speech, Signal Process.*, vol. 38, no. 11, pp. 2008–2014, Nov. 1990.
- [46] H. Akaike  
A new look at the statistical model identification  
*IEEE Trans. Automat. Control*, vol. 19, no. 6, pp. 716–723, Dec. 1974.
- [47] J. Rissanen  
Modeling by shortest data description  
*Automatica*, vol. 14, pp. 465–471, Sep. 1978.
- [48] E. Fishler and H. V. Poor  
Estimation of the number of sources in unbalanced arrays via information theoretic criteria  
*IEEE Trans. Signal Process.*, vol. 53, no. 9, pp. 3543–3553, Sep. 2005.
- [49] F. Foroozan and A. Asif  
Cramer-Rao bound for time reversal active array direction of arrival estimators in multipath environments  
in *Proc. IEEE Int. Conf. Acoust., Speech Signal Process.*, Mar. 2010, pp. 2646–2649.
- [50] R. A. Monzingo, R. L. Haupt, and T. W. Miller  
*Optimum Array Processing*. London, U.K.: IET Digital Library, 2011.
- [51] S. Popoff, G. Lerosey, R. Carminati, M. Fink, A. Boccara, and S. Gigan  
Measuring the transmission matrix in optics: An approach to the study and control of light propagation in disordered media  
*Phys. Rev. Lett.*, vol. 104, no. 10, Mar. 2010, Art. no. 100601.
- [52] Y. Mehmet and F. Shanhai  
Time reversal of light with linear optics and modulators  
*Phys. Rev. Lett.*, vol. 93, no. 17, Oct. 2004, Art. no. 173903.
- [53] R. Carminati, R. Pierrat, J. Rosny, and M. Fink  
Theory of the time reversal cavity for electromagnetic fields  
*Opt. Lett.*, vol. 32, no. 21, pp. 3107–3109, Nov. 2007.
- [54] D. Liu, S. Vasudevan, J. Krolik, G. Bal, and L. Carin  
Electromagnetic time-reversal source localization in changing media: Experiment and analysis  
*IEEE Trans. Antennas Propag.*, vol. 55, no. 2, pp. 344–354, Feb. 2007.
- [55] J. Liu, B. Yuan, and X. Ming  
The CRB on wideband direction of arrival estimation under the background of colored noises  
in *Proc. 2nd Int. Conf. Power Electron. Intell. Transp. Syst.*, Dec. 2009, vol. 1, pp. 416–419.
- [56] L. V. Blake  
*Radar Range-Performance Analysis*. Lexington, KY, USA: Lexington Books, 1980.
- [57] T. Lo and J. Litva  
Use of a highly deterministic multipath signal model in low-angle tracking  
*Inst. Elect. Eng. Proc. F-Radar Signal Process.*, vol. 138, no. 2, pp. 163–171, Apr. 1991.
- [58] A. J. Weiss and B. Friedlander  
Effects of modeling errors on the resolution threshold of the MUSIC algorithm  
*IEEE Trans. Signal Process.*, vol. 42, no. 6, pp. 1519–1526, Jun. 1994.
- [59] R. Hamza and K. Buckley  
An analysis of weighted eigenspace methods in the presence of sensor errors  
*IEEE Trans. Signal Process.*, vol. 43, no. 5, pp. 1140–1150, May 1995.
- [60] H. Gene and F. V. Charles  
*Matrix Computation*. Baltimore, MD, USA: The Johns Hopkins Univ. Press, 2013.
- [61] R. A. Horn and C. A. Johnson  
*Matrix Analysis*. Cambridge, U.K.: Cambridge Univ. Press, 1985.



**Xiaolu Zeng** received the B.S. degree in electrical and information engineering from the Harbin Institute of Technology, Harbin, China, in 2014. He is currently working toward the Ph.D. degree in signal and information processing at the School of Electronic Engineering, Xidian University, Xi'an, China.

Since September 2017, he has been a Visiting Student with the Department of Electrical and Computer Engineering, University of Maryland, College Park, MD, USA, with the support of China Scholarship Council. His current research interests include array signal processing, multipath exploration using time reversal technique, parameter estimation, time-reversal-based wireless communication, target detection, localization, tracking, and classification.



**Minglei Yang** (M'14) received the B.E. degree in electronic engineering and the Ph.D. degree in signal and information processing from Xidian University, Xi'an, China, in 2004 and 2009, respectively.

Since 2009, he has been with the National Laboratory of Radar Signal Processing, Xidian University, where he is currently an Associate Professor. From 2014 to 2015, he was a Visiting Scholar at the Elisha Yegal Bar-Ness Center for Wireless Communications and Signal Processing Research at the New Jersey Institute of Technology. His research interests include the fields of array signal processing, MIMO signal processing, and polarization information processing. He have published more than 80 peer-reviewed journals and conference papers and more than 40 inventions.



**Baixiao Chen** was born in Anhui, China, in 1966. He graduated from Metallurgy College of East China, Ganzhou, China, in 1987 and worked there from Jul. 1987 to Jul. 1991, and the Master degree in circuit and system and the Ph.D. degree in signal and information processing from Xidian University, Xi'an, China, in 1994 and 1997, respectively.

He was with Metallurgy College of East China from July 1987 to July 1991. Since 1997, he has been a Faculty Member with the National Laboratory of Radar Signal Processing, Xi'an, China. He was a Lecturer and an Associate Professor from October 1997 to May 1999 and from June 1996 to May 2003, respectively. In 2006, he was selected into “New Century elitist Support Program” of the Ministry of Education. He is currently a Professor of signal and information processing at Xidian University. His general research interests include radar signal processing, new radar system design, array signal processing, precision guidance, etc.



**Yuanwei Jin** (S'99–M'04–SM'08) received the Ph.D. degree in electrical and computer engineering from the University of California at Davis, Davis, CA, USA, in 2003.

He is currently a Professor in electrical engineering and the Chair of the Department of Engineering and Aviation Sciences with the University of Maryland Eastern Shore (UMES), Princess Anne, MD, USA. Prior to joining UMES, he was a Postdoctoral Research Fellow and then a Project Scientist with the Department of Electrical and Computer Engineering, Carnegie Mellon University, Pittsburgh, PA, USA. He holds four U.S. patents. His research interests include signal processing, sensor array processing, and inverse problems, with applications in radar/sonar, biomedical imaging, wireless communications, structural health monitoring, and nonintrusive loading monitoring for smart facilities.

Dr. Jin was a recipient of the 2016 BEYA Special Recognition Award on educational leadership in the 2016 BEYA-STEM conference and the 2010 Air Force Summer Faculty Fellowship Award. He was a recipient of an Earle C. Anthony Fellowship from the University of California at Davis. He is affiliated with several IEEE societies, SPIE, and the American Society for Engineering Education.